2024-12-04

Nonlinear Thomson Scattering in an Intense Tightly Focused Ultrashort Laser Pulse

Yance Sun
Brigham Young University

Nonlinear Thomson Scattering in an Intense Tightly Focused Ultrashort Laser Pulse

Yance Sun

A thesis submitted to the faculty of
Brigham Young University
in partial fulfillment of the requirements for the degree of

Master of Science

Justin Peatross, Chair
Michael Ware
Chris Verhaaren

Department of Physics and Astronomy

Brigham Young University

ABSTRACT

Nonlinear Thomson Scattering in an Intense Tightly Focused Ultrashort Laser Pulse

Yance Sun
Department of Physics and Astronomy, BYU
Master of Science

We investigate nonlinear Thomson scattering generated by intense laser pulses focused in noble gases. Electrons are ionized from low-density helium or argon early during the laser pulse and scatter light out the side of the focus. We measure fundamental, second, and third harmonic light focus over nearly the entire emission sphere. We investigate the influence of electron bunching, when individual atoms ionize multiple electrons sequentially as the laser field increases early during the laser pulse. Simulations suggest that correlation between electron positions for the ten electrons ionized from argon should distort the spatial pattern of nonlinear Thomson scattering relative to the two-electron pattern observed for helium. Preliminary experimental measurements do not reveal a difference in emission patterns between helium and argon. However, our experimental efforts were hampered by prepulses in our laser system, which could cause electrons to ionize ahead of the main pulse and disrupt the coherence between electrons. In the future, we hope to improve the pulse temporal contrast of the laser system and revisit this experiment.

We also explore observed distortions in the angular emission patterns of nonlinear Thomson scattering. These persistent distortions arise presumably from subtle defects in the laser field, which can imprint on the angular distribution of the scattered light. Possibilities include variations in laser focal shape, spatial chirp, and laser-field polarization. We set out on a systematic experimental course to identify laser beam characteristics that may contribute to such distortions in the angular emission patterns. We develop experimental tests which have implicated our wave plate, used to rotate linear laser polarization, as a likely source of distortion. Further tests on the wave plate are required to confirm and explain how it affects the angular distribution of nonlinear Thomson scattering.

Keywords: nonlinear Thomson scattering, angular emission patterns, high intensity, ultrashort laser pulses, coherence of ionized electrons

ACKNOWLEDGMENTS

Thank you to the BYU Physics and Astronomy Department and Dr. Peatross for giving me the opportunity to be a graduate student. I am grateful for the Church of Jesus Christ of Latter-Day Saints and Dr. Peatross for my spiritual guidance. Thanks to my big supporters: my wife, parents, and in-laws. Finally, I extend my profound gratitude to all the professors in the physics department, specifically Dr. Peatross, Dr. Ware, and Dr. Verhaaren.

Contents

Chapter 1

Introduction

1.1 Linear Thomson Scattering

J. J. Thomson confirmed the existence of electrons in 1897 and later made the first calculation of how electrons scatter light in the presence of an incident light field [1]. Thomson's calculation may be viewed as the long wavelength limit of Compton scattering [2]. Thomson's original formulation applies when the light intensity is low, which was always the case until advances in laser technology during the 1980s.

Thomson scattering can be modeled using the relativistic equation of motion for an electron of charge q driven by an electric field $\mathbf{E}$ and magnetic field $\mathbf{B}$, given by by

$$\frac{d\mathbf{p}}{dt} = q\left(\mathbf{E} + \cancelto{0\text{ TS}}{\mathbf{u}\times\mathbf{B}}\right) , \tag{1.1}$$

where $\mathbf{u}$ is the electron velocity and $\mathbf{p}$ is the electron momentum:

$$\mathbf{p} = \gamma m_e \mathbf{u} \quad \text{and} \quad \gamma = \frac{1}{\sqrt{1 - \cancelto{0\text{ TS}}{u^2/c^2}}} . \tag{1.2}$$

Terms with an arrow drawn through them in this analysis vanish in the low-intensity limit of linear Thomson scattering (TS) but are retained for nonlinear Thomson scattering. For linear Thomson scattering, Eq. (1.1) simplifies to $\mathbf{a} \equiv \frac{d\mathbf{u}}{dt} = \frac{q\mathbf{E}}{m_e}$, where $\mathbf{a}$ is the ordinary electron acceleration. For an incident plane-wave field (representing a laser), with frequency ω, amplitude E_0, and linear polarization (along $\hat{\mathbf{x}}$), we may write

$$\mathbf{E} = \hat{\mathbf{x}} E_0 \cos(\omega t) \quad \text{and} \quad \mathbf{B} = \hat{\mathbf{y}} \frac{E_0}{c} \cos(\omega t) \; . \tag{1.3}$$

In the case of linear Thomson scattering, the electron undergoes sinusoidal acceleration

$$\mathbf{a} = \hat{\mathbf{x}} \frac{qE_0}{m_e} \cos(\omega t) \; . \tag{1.4}$$

Thomson computed light scattered into the *far field*, presumably to a distant detector at position $\mathbf{r}_d = r_d \hat{\mathbf{r}}_d$, illustrated in Fig. 1.1. In general, the electric and magnetic fields radiated by a charged particle is [3]

$$\mathbf{E}_S(\mathbf{r}_d, t_d) = \frac{q}{4\pi\varepsilon_0 c^2 r_d} \frac{\left(\hat{\mathbf{r}}_d - \cancelto{0\ TS}{\mathbf{u}/c}\right) \times \mathbf{a}}{\left(1 - \cancelto{0\ TS}{\hat{\mathbf{r}}_d \cdot \mathbf{u}/c}\right)^3} \quad \text{and} \quad \mathbf{B}_S(\mathbf{r}_d, t_d) = \frac{1}{c} \hat{\mathbf{r}}_d \times \mathbf{E}_S(\mathbf{r}_d, t_d) \; , \tag{1.5}$$

where

$$t_d = t + r_d/c - \cancelto{0\ TS}{\hat{\mathbf{r}}_d \cdot \mathbf{r}/c}, \tag{1.6}$$

is the time at the detector when the field is measured, and $\mathbf{r}$ is the position of the electron at time t. All quantities on the right-hand side of Eq.(1.5) for $\mathbf{E}_S$ are evaluated at time t, whereas the field arriving at the detector is specified at time t_d. Note that for linear Thomson scattering, certain terms in the above expressions are ignored, assuming non relativistic electron velocity.

The intensity of the radiated light is derived from the Poynting vector:

$$\mathbf{S} = \mathbf{E}_S \times \frac{\mathbf{B}_S}{\mu_0} \; . \tag{1.7}$$

Note that in the above expressions we have ignored the possible influence of the scattered field on the electron trajectory. For our laser conditions, radiation reaction force is negligible. This classical treatment, which decouples incoming and outgoing radiation, would be wholly inadequate for describing Compton scattering, where an electron can recoil with significant momentum when scattering x-ray photon. However, this approximation is appropriate in the long-wavelength limit of Thomson scattering [2]. As depicted in Fig. 1.1, we can specify the direction to the detector in

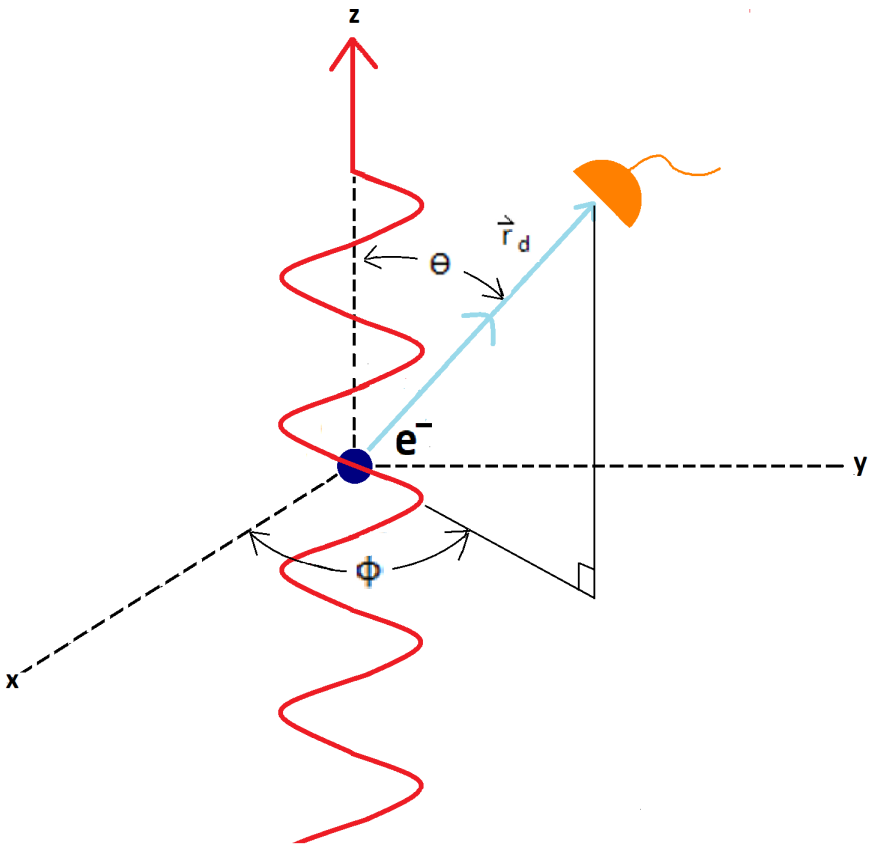

Figure 1.1 In a far field approximation, the electron is close to the origin and the detector is far from the origin.

terms of angles in spherical coordinates:

$$\hat{\mathbf{r}}_d = \hat{\mathbf{x}}\sin\theta\cos\phi + \hat{\mathbf{y}}\sin\theta\sin\phi + \hat{\mathbf{z}}\cos\theta\ . \tag{1.8}$$

Here, θ is the usual polar angle, and ϕ is the azimuthal angle.

To compute linear Thomson scattering, we substitute Eqs.(1.4) and (1.8) into the expressions for the fields in Eq. (1.5). The time average of the magnitude of the Poynting vector, called intensity, becomes (1.7):

$$I_S = \langle S \rangle_t = \frac{1}{2}\varepsilon_0 c \left(\frac{q^2 E_0}{4\pi m c^2 \varepsilon_0 r_d} \right)^2 \left[\cos^2\theta + \sin^2\theta \sin^2\phi \right] . \tag{1.9}$$

This is the well-known formula for *linear* Thomson scattering, when the electron responds to an incident field linearly polarized along the x direction. A graph of the radiated intensity is shown in Fig. 1.2. (If we had chosen the light polarization to lie in the z-direction, then the factor in square

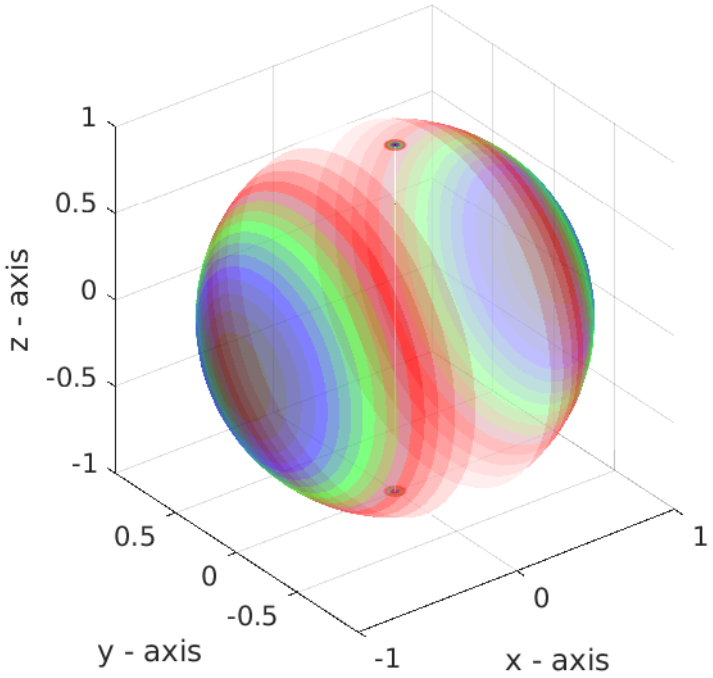

Figure 1.2 The intensity spectrum of stimulated electron emission from simple plane wave in x-direction.

brackets would simply be $sin^2\theta$, which is the way it usually appears in textbooks [3].) Later in this thesis, it will be convenient to have the incident laser field propagate in the z direction, with its linear polarization aligned along the x direction.

We can integrate over the entire emission sphere to find the total radiated power: $P = \sigma I_0$, where $I_0 = \frac{1}{2}\varepsilon_0 c E_0^2$ is the intensity of the incident field and $\sigma = \frac{\mu_0^2 q^4}{6\pi m^2} = 6.65 \times 10^{-25}$ cm^2 is the linear Thomson scattering cross section. From this, we can estimate the number of photons radiated from an electron that experiences a laser pulse. As an example, according to the linear Thomson scattering formula, an electron experiencing our 40 fs laser pulses with intensity around 10^{18} W/cm^2 would scatter $\mathscr{E} = \left(40 \times 10^{-15}\text{ s}\right)\left(10^{18}\text{ W/cm}^2\right)\left(6.65 \times 10^{-25}\text{cm}^2\right)\frac{1\text{ eV}}{1.602 \times 10^{-19}\text{ J}} = 0.17$ eV. Our laser photon energy is 1.55 eV, so we might expect one photon to scatter (within the angular scattering distribution) from a single electron about once in every ten laser shots. However, our laser intensity is much too high for the approximations used to derive linear Thomson scattering. We must redo the calculations while retaining the neglected terms in the above equations.

1.2 Nonlinear Thomson Scattering

When retaining the various terms previously neglected in the above calculations, Thomson scattering becomes *nonlinear*. Instead of oscillating sinusoidally in a plane wave field, an electron follows a more complicated trajectory. In 1951, Landau and Lifshitz showed that an electron follows a figure-8 path when driven by a sufficiently strong linearly polarized plane wave field [4]. In 1962, Vachaspati showed that an electron executing such a trajectory radiates both even and odd harmonics of the driving field [5]. In 1968, Eberly and Sleeper showed that the electron is also pushed forward by the laser, so in the lab frame, the motion resembles a triangular wave [6]. 1970, Sarachik and Shappert published a comprehensive theoretical treatment of nonlinear Thomson scattering [7]. In addition to responding to the electric field, the the electron is also pushed by the magnetic field

along the dimension of laser propagation, z. Nevertheless, the electron oscillates primarily along the polarization direction with speeds approaching but bounded by c. The rising edge of the laser pulse causes the electron to drift in the forward direction of the incident field as it executes a figure-8 motion in the XZ plane.

Figure 1.3 shows the path that an electron takes in a plane-wave pulse that is strong enough to cause relativistic electron motion. The peak field was chosen to be $E_0 = m_e c\omega/q$, which demarcates the onset of relativistic effects (i.e. electron velocity reaching 0.9c). For our 800 nm laser, this corresponds to a peak intensity of $I_0 = \frac{1}{2}\varepsilon_0 c E_0^2 = 2.1 \times 10^{18}$ W/cm^2. The electron path was computed by numerically integrating Eqs. (1.1) – (1.3), where the field strength E_0 was multiplied by a temporal pulse envelope $e^{-\frac{t^2}{\tau^2}}$, with $\tau = 34$ fs. The figure-8 shape is actually only seen in the average rest frame of the electron; in the lab frame, the electron path looks more like a saw-tooth wave as seen in Fig. 1.3(b).

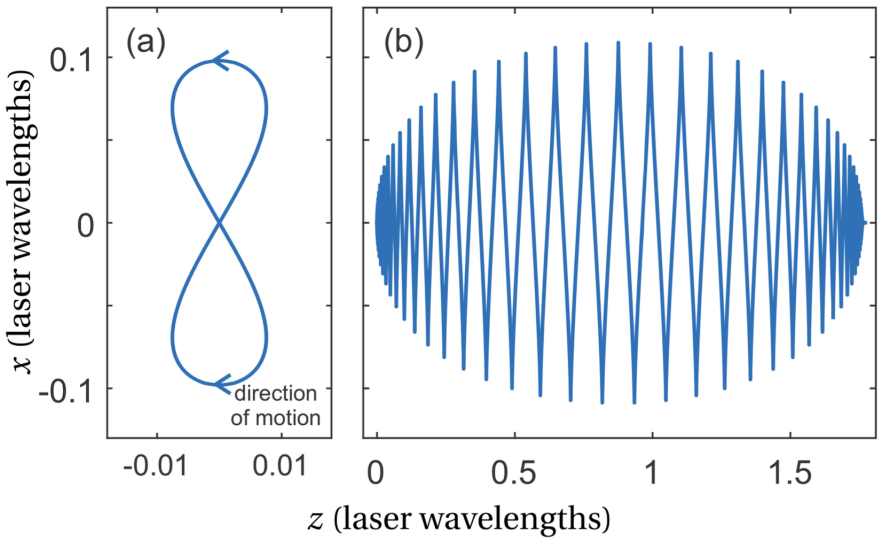

Figure 1.3 Graphic reproduced from Ref. [8]. (a) Trajectory path for an electron experiencing nonlinear Thomson scattering in average rest frame for a single cycle near the peak of the pulse. (b) Trajectory path for an electron experiencing a laser pulse that is about a dozen cycles in duration (lab frame).

An electron undergoing the motion shown in Figs. 1.3 radiates light according to Eq. (1.5). Since the motion is nonlinear, new frequencies are part of the resulting radiation. Fig. 1.4 shows the calculated intensity due to nonlinear Thomson scattering using the formula developed by Sarachik and Shappert. Fundamental, second harmonic, and third harmonic light is shown in the far field, resolved into two polarization states (i.e. along $\hat{\theta}$ and $\hat{\phi}$ directions). Higher order harmonics are also generated with less amplitude (not shown).

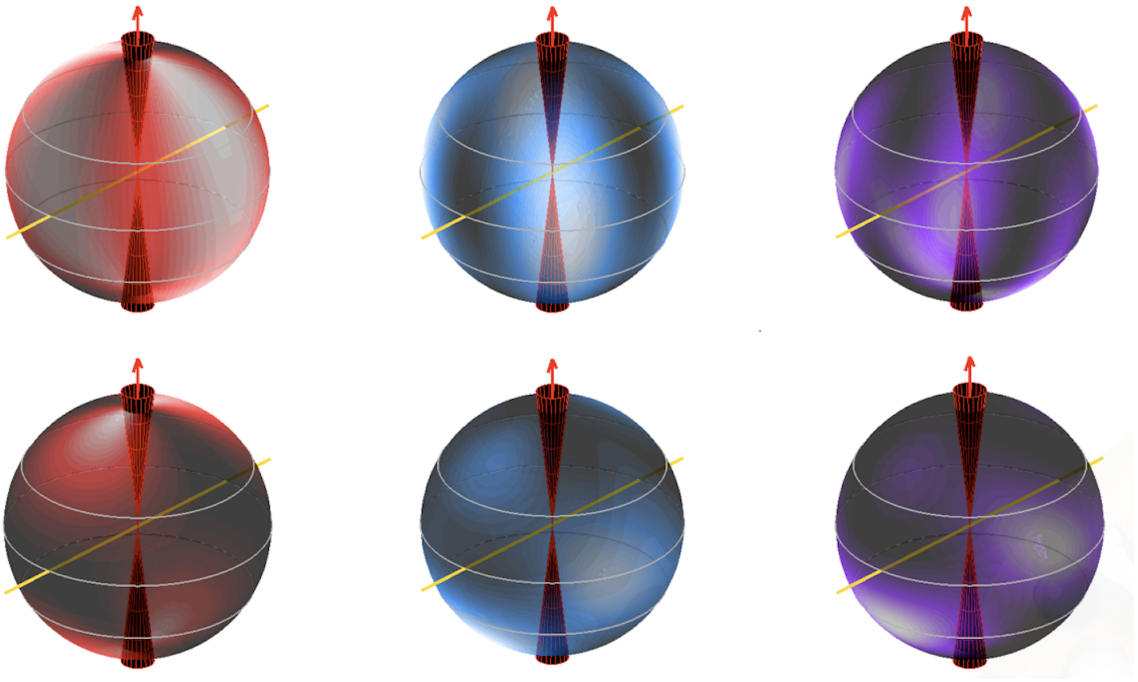

Figure 1.4 Total intensity of fundamental (left), second and third harmonics (right) for the azimuthal(top) and longitudinal(bottom) polarization components of nonlinear Thomson scattering. The yellow line indicates the direction of linear polarization of the incident field.

For a more realistic laser focus, instead of using Eq. (1.3), we model the electric vector field of a tightly focused laser using [9, 10]

$$\mathbf{E} = \mathrm{Re}\left\{ E_0 e^{-\left(\frac{\bar{\varphi}}{\omega\tau}\right)^2} \left(\hat{\mathbf{x}} + \frac{xy}{2\mathbb{Z}^2}\hat{\mathbf{y}} - i\frac{x}{\mathbb{Z}}\hat{\mathbf{z}} \right) \frac{z_0}{\mathbb{Z}} e^{-\frac{kz_0\rho^2}{2|\mathbb{Z}|^2}} e^{i\bar{\varphi}} \right\}, \tag{1.10}$$

where $\mathbb{Z} = z_0 + iz$ and $\tilde{\varphi} = kz[1 + \rho^2/(2|\mathbb{Z}|^2)] - \omega t$. z_0 is the Rayleigh range, ρ the axial radius, and τ the pulse duration. The associated magnetic field is $c\mathbf{B} = \hat{\mathbf{x}}E_y + \hat{\mathbf{y}}E_x + \hat{\mathbf{z}}\frac{y}{x}E_z$.

In a tight laser focus (with focal radius $w_0 = 44\,\mu\text{m}$ and $z_0 = \frac{\pi w_0^2}{\lambda} = 63\,\mu\text{m}$), electron trajectories become strongly distorted, compared to trajectories in a plane wave, as they are propelled out the side of the focus by the strong field gradient during the laser pulse. Surprisingly, the computed radiation from a large ensemble of electrons randomly distributed throughout the laser focus looks similar to the radiation pattern from a single electron in a plane wave pulse. A typical laser beam profile is shown within each sphere of Fig. 1.4.

1.3 Experimental Measurements

In 1998, Chen *et al.* first measured second and third harmonics produced by nonlinear Thomson scattering in a high intensity laser. [11] They measured the second and third harmonics along the equator and one other latitude of spheres shown in Fig. 1.4.

In 2021, the group of Peatross and Ware at BYU first published measurements of polarization-resolved fundamental, second, and third harmonic nonlinear Thomson scattering [12]. They observed nonlinear Thomson scattering out the side of a high intensity laser focus. The separate measured polarization components are each associated with a distinct dimension of predicted electron figure-8 motion. Taken together, the measured angular emission patterns for the two polarizations confirm two-dimensional motion consistent with the figure-8 shape.

This past year, I participated in the first measurements of polarization-resolved fundamental, second and third harmonic nonlinear Thomson scattering over nearly the full emission sphere. [13] The experimental setup is shown in Fig. 1.5.

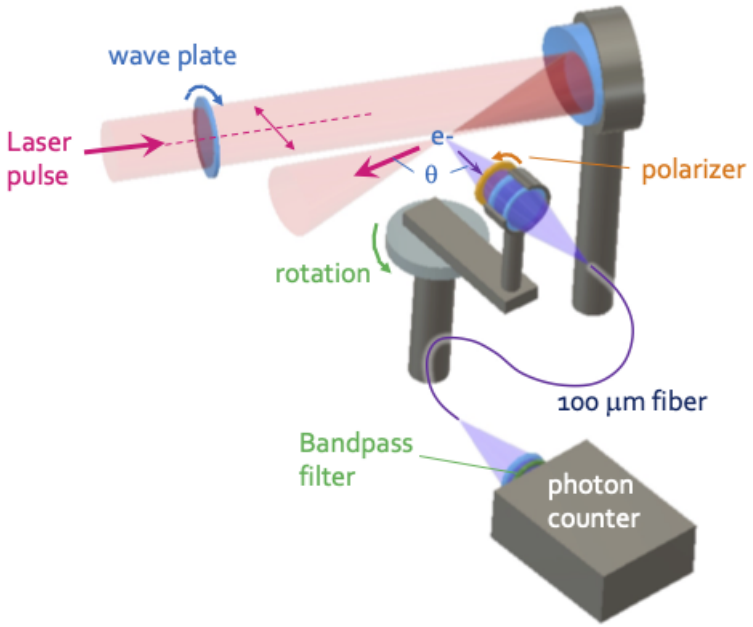

Figure 1.5 Experimental setup for nonlinear Thomson scattering measurements. A half wave plate prior to the parabola rotates the linear polarization of the laser beam. The off-axis parabola focuses the incident laser beam. Scattered photons go through a polarizer, after which an achromatic lens pair focus the signal into an optic fiber.

The new data show, for the first time experimentally, emission structure in the 'Northern' and 'Southern' hemispheres, where the 'North Pole' aligns with the direction of laser propagation. With this new data, we can tell which direction electrons move around the figure 8 race track. Measurements of the fundamental, second, and third harmonic are shown in Figs. 1.6, 1.7, and 1.8.

For our experimental setup, laser pulses are focused using an off-axis parabola to a spot with $w_0 = 3.2\,\mu\text{m}$. A half wave plate prior to the parabola rotates the linear polarization of the laser beam. In our analysis, we always choose the x axis to be along the laser polarization. Our laser delivers about 50 mJ in 40 fs. This achieves an estimated 2×10^{18} W/cm^2 peak intensity in the focus.

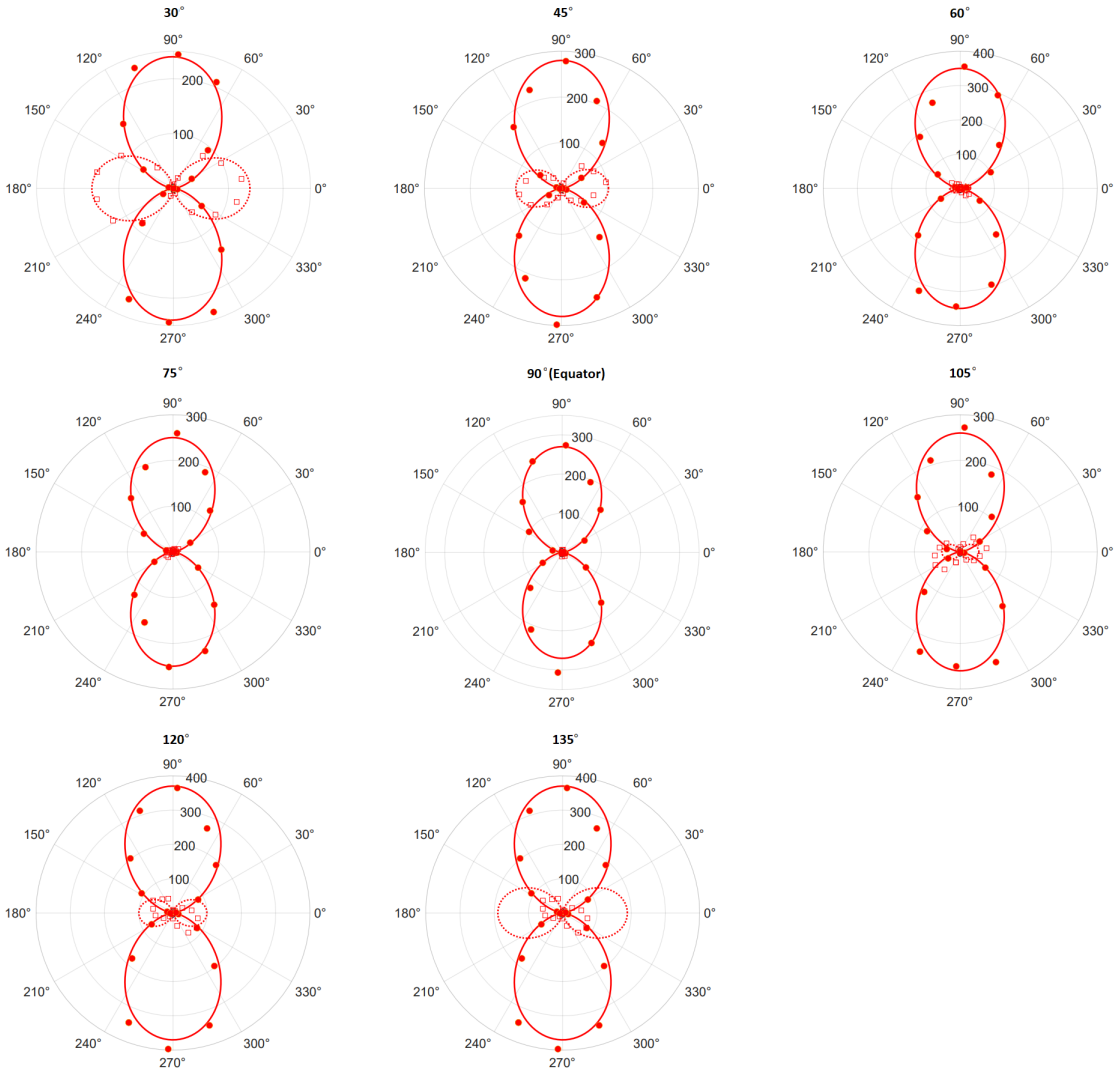

Figure 1.6 Intensity in the planes at degrees of 30(top left), 45, 60, 75, 90, 105, 120, 135(bottom right) the azimuthal (solid) and longitudinal (dashed) components of the fundamental harmonics.

Free electrons are donated from low-density helium back-filled in the chamber that houses the experiment. Typical pressures are 10^{-4} Torr when measuring the fundamental, 10^{-2} Torr when measuring the second harmonic, and 1 Torr when measuring the third harmonic. The helium is ionized early during the laser pulse, at intensities several orders of magnitude below the peak intensity.

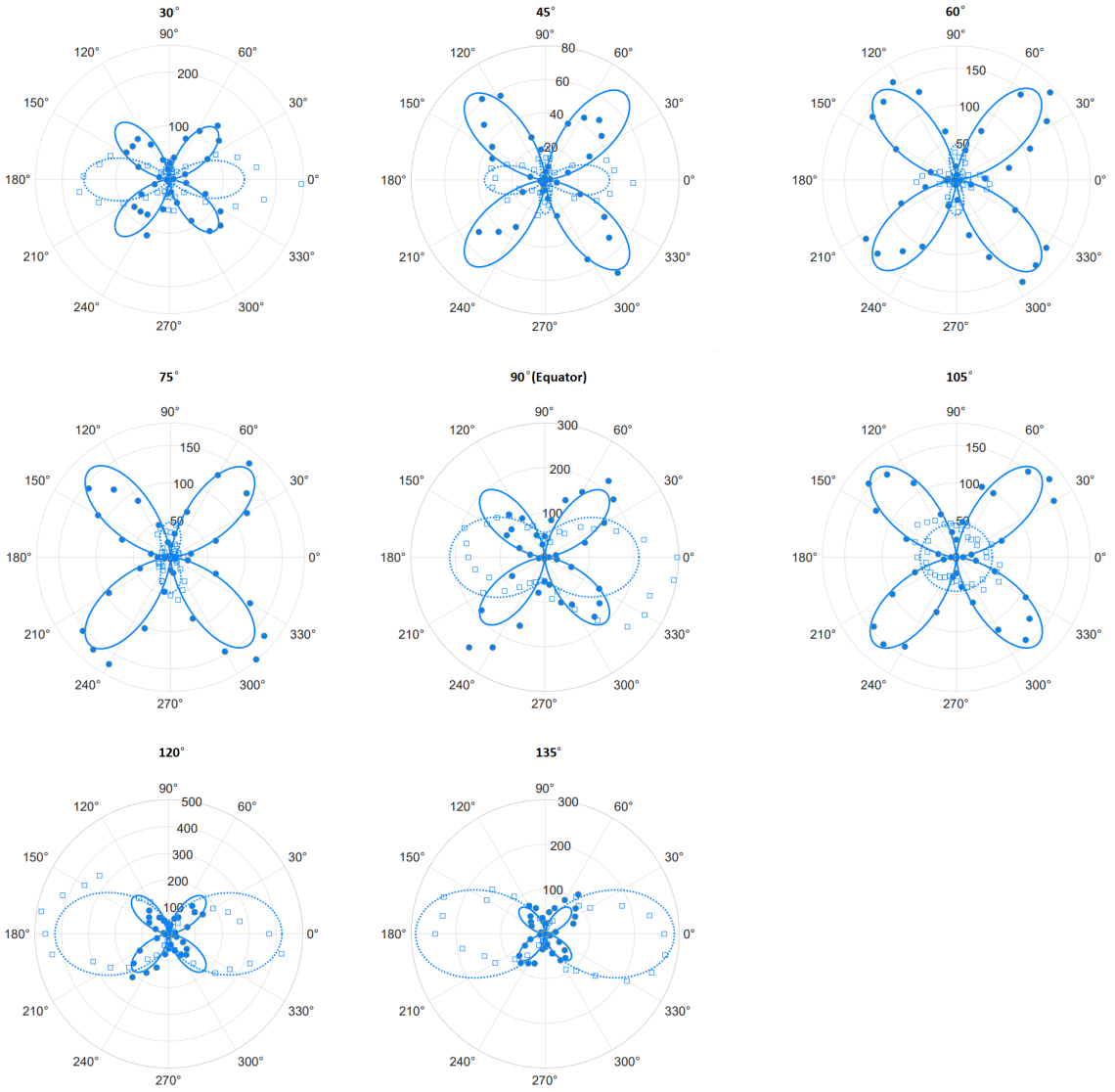

Figure 1.7 Intensity in the planes at $\theta = 30°$ (top left), 45°, 60°, 75°, 90°, 105°, 120°, 135° (bottom right) the azimuthal (solid) and longitudinal (dashed) components of the second harmonics.

Individual photons are detected using a photon counter, and detector counts are accumulated from 600 laser shots. The solid and dashed curves in Figs. 1.6, 1.7, and 1.8 correspond to simulations of photons detected through orthogonal polarizer orientations. The data in Figs. 1.6, 1.7, and 1.8 trace out 'latitude' lines around the emission sphere, at various angles from the 'North Pole'. For example, the curve at 60°, 90°, and 120° correspond to traces around the gray lines in Fig. 1.4.

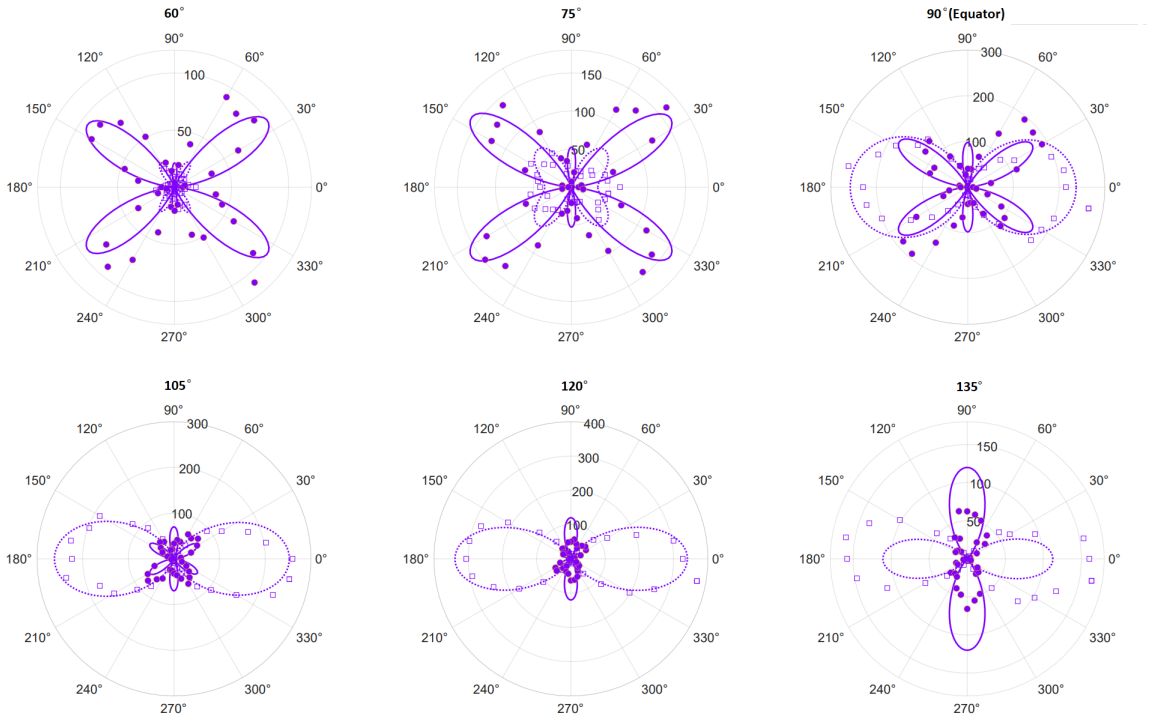

Figure 1.8 Intensity in the planes at degrees of 60 (top left), 75, 90, 105, 120, 135 (bottom right) the azimuthal (solid) and longitudinal(dashed) components of the third harmonics.

A clear asymmetry between emission into the 'Northern' and 'Southern' hemispheres can be seen for the longitudinal polarization. This demonstrates that the electron whips around the two ends of the figure-8 in the direction opposite to the direction of laser propagation. This is the first experimental demonstration that the electron motion is 1) two-dimensional in the XZ plane and 2) moves opposite the laser propagation on both ends of its motion.

1.4 Overview

In extreme light conditions, the nonlinear interaction between electrons and the laser field produces harmonic radiation. In principle, this scatter carries detailed information about the spatial and temporal profile of the laser focus. Understanding these scattering dynamics has the potential to help optimize laser systems for applications like particle acceleration, fusion compression, high-energy physics experiments, and advanced imaging techniques, where precise control of laser intensity and focus is essential.

This thesis reports on the work published in three journal publications, two published in 2024 and one published while I was still an undergraduate at BYU [8, 13, 14]. I collected the third harmonic data in Fig. 1.8. I have performed preliminary work in two new directions related to the above experiments. First, I have investigated the possibility of coherence effects between electrons ionized from the same atom as they execute subsequent relativistic motion and emit nonlinear Thomson scattering. We have studied the effect theoretically [14] and have attempted to see it experimentally. These experimental efforts were hampered by pulse temporal contrast in our laser system. We made progress in reducing the strength of prepulses that could prematurely ionize the helium in our laser focus, allowing electrons to de-cohere. Further improvements to laser pulse contrast will be necessary to see this effect. Our theoretical analysis of multi-electron coherence effects in Thomson scattering and our experimental efforts made so far, as well as our plans for laser pulse cleaning, are described in chapter 2.

In a second project, I explored distortions in the angular distributions of nonlinear Thomson scattering. Our original goal was to evaluate how distortions in our high-intensity laser focus might translate into asymmetries in the patterns seen in Figs. 1.6, 1.7, and 1.8. That is, we wanted to know how spatial chirp or astigmatism, for example, may lead to alterations in how electrons are propelled out the sides of the laser focus by the strong field. They could exit the focus along preferred directions, which could imprint on the measured nonlinear Thomson scattering emission patterns.

For this project, it was necessary to first produce the cleanest possible spatially symmetric laser focus. We were surprised that after our best efforts, the angular emission patterns of the nonlinear Thomson scattering showed marked asymmetries, indicated that unknown effects were at play as well. We set out on a systematic experimental course to identify all laser-beam characteristics that could introduce distortions in the the angular emission patterns. We have narrowed down the possibilities considerably, but the underlying cause is remarkably subtle. These efforts and results are described in chapter 3.

Chapter 4 outlines future work designed to overcome the hurdles in our efforts to measure both coherence effects and sensitivity of nonlinear Thomson scattering to distortions in the laser focus, as outlined above. These efforts have the potential to lead to several additional journal publications. In addition, I described other future experiments to try to measure higher order harmonics, and to look at nonlinear Thomson scattering using colliding laser pulses.

Chapter 2

Coherence Effects from Multi-Electron Ionization

2.1 Simulation of Coherence in Nonlinear Thomson Scattering

In the analysis of nonlinear Thomson scattering, such as highlighted in chapter 1, we summed incoherently the emission from liberated electrons without regard for the common initial positions of electron pairs ionized from individual helium atoms during the early part of the laser pulse. Here, we consider how coherence effects between multiple electrons ionized from the same atom might influence emitted nonlinear Thomson scattering. The possibility that the ionization process imprints coherence effects in the subsequent photoemission may provide a new window into strong-field ionization. For example, whether the probability that an electron emerges from an atom is spread over several laser cycles or is more abrupt might impact the coherence.

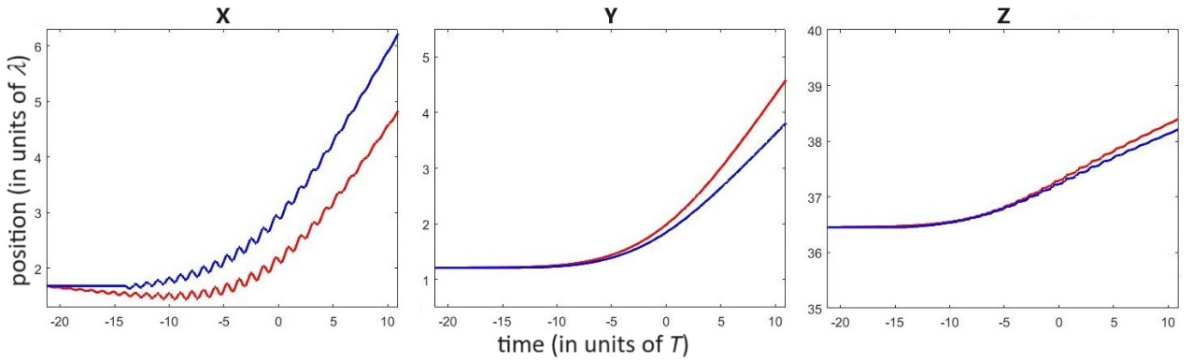

Figure 2.1 Reproduced from Ref. [14]. Trajectories along the separate axes of two electrons (first red, second blue) coming out from the same helium atom. The laser propagates in the z direction and in polarized along the x direction.

In a recent paper [14], we explored the extent to which coherence between multiple electrons ionized from the same atom should influence the angular emission of nonlinear Thomson scattering. We expect that electrons emerging from the same atom are correlated spatially since it takes time for them to move apart. If their separation remains small compared to the scattered wavelength, then the radiation should constructively interfere.

To date, we have mainly used helium as the source of free electrons. Each helium atom donates two electrons, the first breaking free from the atom around 1×10^{15} W/cm^2 and the second around 9×10^{15} W/cm^2 [6]. These intensities occur very early on during the laser pulse since the peak intensity eventually reaches 2×10^{18} W/cm^2. Figure 2.1 shows trajectories for two electrons ionized from a helium atom based on Eqs. (1.1), (1.2), and (1.10). The two electrons are released with zero initial speed at the two ionization intensities noted above. The two electrons separate on the scale of a laser wavelength during the leading edge of the laser pulse as they are pushed out the side of the laser focus while also being pushed down stream. This simulation suggests that it is easy for the positions of electrons born of the same atom to decohere during the laser pulse.

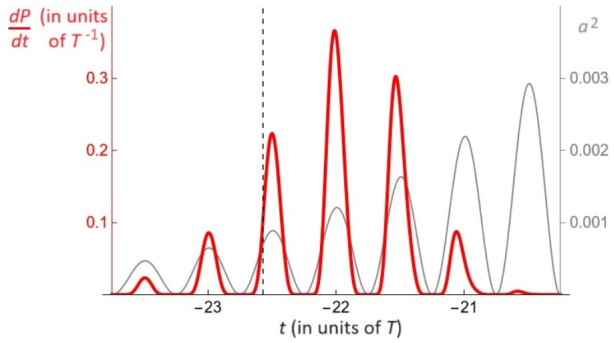

Figure 2.2 Reproduced from Ref. [14]. Probability per time (thick red line), for the first ionization of helium using the ADK model. The thin gray line represents the instantaneous intensity expressed in terms of the dimensionless quantity $\left(\frac{qE_0}{m_e c\omega}\right)^2$. The dashed vertical line marks the instant when ionization would occur classically when sufficient suppression of the Coulomb barrier is achieved. Time is in units of laser periods T with $t = 0$ corresponding to the peak of the laser pulse.

Ionization is a probabilistic process, so one cannot predict and exact intensity or moment when an electron is liberated from an atom by a laser field. A more realistic ionization model by Amazov, Delone, and Krainov [15] (ADK) is shown in Fig. 2.2.The figure shows the probability rate of electron ionization during several laser cycles while the laser field increases early on during our laser pulse. This spreading out of the ionization probability over time has the effect of further de cohering the position of multiple liberated electrons.

Figure 2.4 shows calculated angular emission patterns in the plane perpendicular to the laser focus, computed for an instantaneous model of ionization and for the ADK model. The simulation shows emission patterns for both azimuthal and longitudinal detector polarizations. The emission patterns are computed from electrons emerging from helium atoms randomly positioned through the interaction region. These simulations were performed by our collaborator Prof. Sá of the University of the Azores. The simulation applies bandpass filters centered on slightly redshifted wavelengths to distinguish different harmonics, similar to those used in our experiments [13].

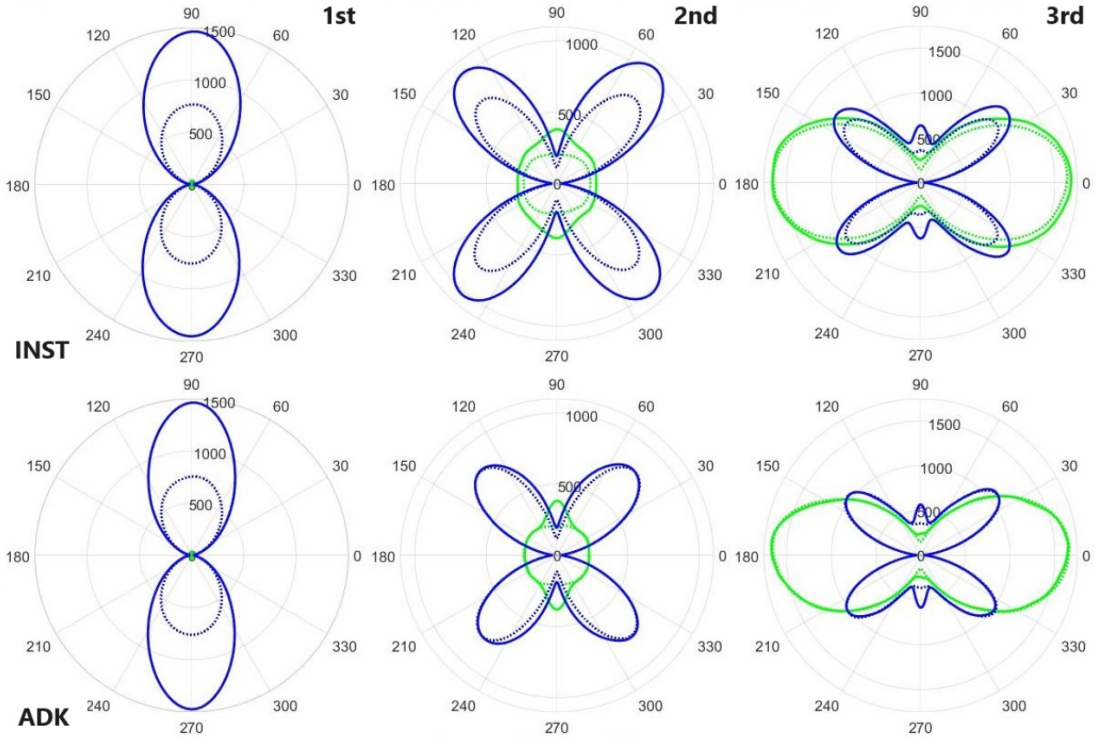

Figure 2.3 Reproduced from Ref. [14]. Calculated angular distributions of the fundamental, 2nd, and 3rd harmonic photon counts scattered by electrons ionized from helium, comparing the instantaneous (upper row) and ADK ionization models (lower row). The plots show scattering in the plane perpendicular to the laser focus using a simulation of 10,000 atoms randomly distributed throughout the interaction region. Blue lines indicate azimuthal polarization and green lines indicate longitudinal polarization of the light reaching the detector. The ADK row is a repeat of the upper row. For comparison, the dotted lines indicate photon counts while ignoring interference (i.e, summing intensities).

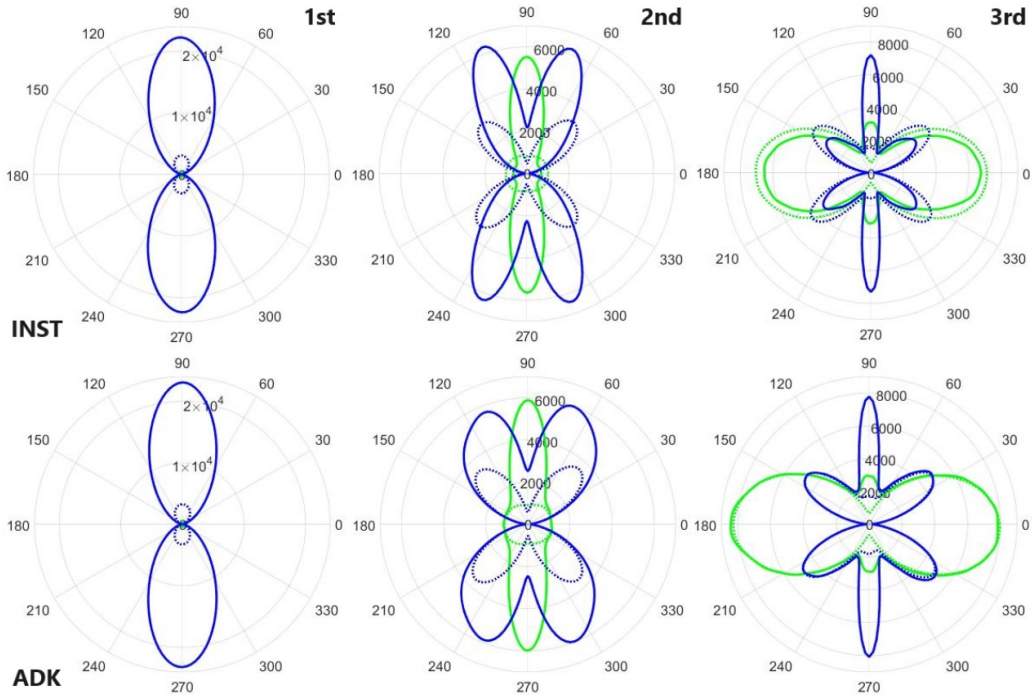

Figure 2.4 Reproduced from Ref. [14]. Same as Fig. 2.3, except computed using argon.

Coherence effects are more pronounced at the longer wavelengths such as the scattered fundamental or the second harmonic. The results also depend mildly on the ionization model chosen. However, the atomic species used can have a significant influence on the angular distribution of scattered photons. Figure 2.4 shows similar calculations made for argon, which can donate up to 10 electrons per atom for our laser intensities.

When comparing Figs. 2.3 and 2.4, the fundamental and harmonics show a strong enhancement of emission from argon over helium along directions perpendicular to the laser polarization. This is expected owing to the larger number of electrons available for ionization in argon and the fact that electrons ionized from the same atom tend to separate mostly along the dimension of the linear laser polarization, owing to the initial condition of zero electron velocity upon ionization.

To appreciate how the instant that an electron is released influences its subsequent trajectory, consider as an example nonrelativistic motion with $F = qE_0 \cos(\omega t + \phi) = m\ddot{x}$, where ϕ is the phase of the laser field when the electron is released from the atom. Integrating, we find the velocity to be $\dot{x} = \frac{qE_0}{m\omega}[\sin(\omega t + \phi) - \sin\phi]$, where an integration constant $-\frac{qE_0}{m\omega}\sin\phi$ is chosen to make the speed zero at $t = 0$. This introduces a drift along the direction of the electric field, which can lead to extra separation between electrons in that dimension. This tends to cause incoherence in subsequent emission along that dimension. On the other hand, it does not to harm coherence in dimensions perpendicular. Figure 2.5 shows the radiation emitted by two electrons, which is in phase and out of phase along two different directions.

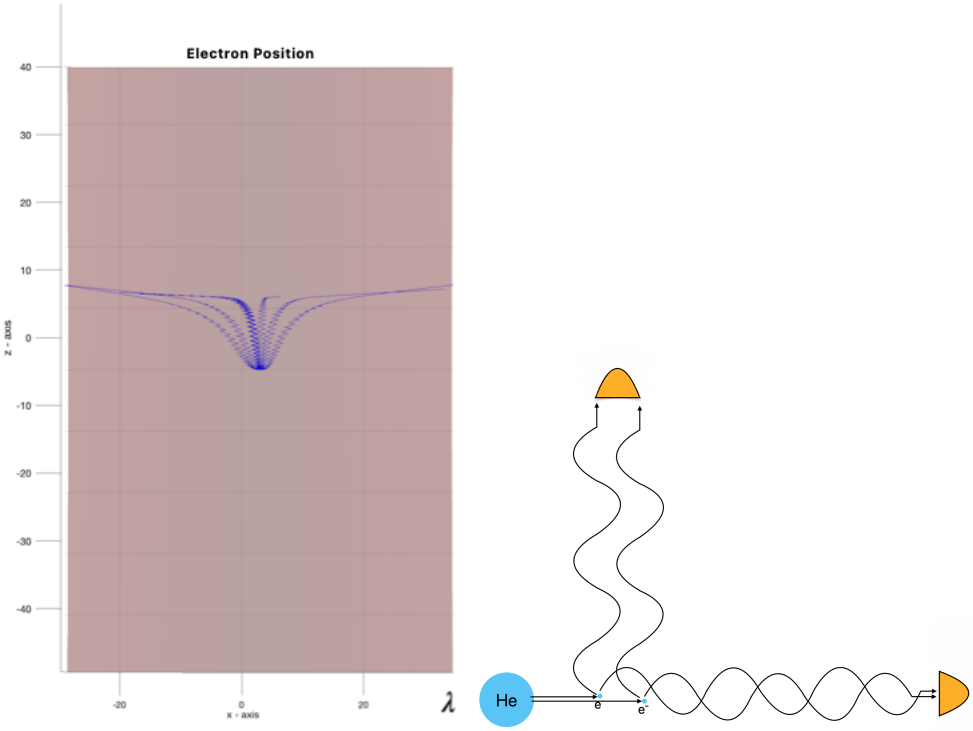

Figure 2.5 Calculate position of multiple electrons ionized from argon during a laser pulse (left), and depiction of laser pulse how radiation from two electrons can exhibit different coherence depending along which direction the electrons separate (right).

Generally, if the emission between all electrons born of the same atom is coherent, then we would expect an increase of approximately $5^2 = 25$ times for argon compared to helium at the same gas density, since there are up to five times more electrons ionized for argon. On the other hand, if the emission is incoherent, then the emission for argon would be only five times higher; this should be observable. As mentioned, the degree of coherence can be different along different dimension, owing to how the electrons spread out. As can be seen in the Fig. 2.4, there is a strong enhancement in emission along the y dimension for argon over helium.

Again, the simulations show a slight dependence on ionization model. These modest variations in the angular emission patterns might be used to try to distinguish between different ionization models.

In summary, our simulations predict measurable coherence effects in nonlinear Thomson scattering from electron bunches born of the same atom in an intense short laser pulse. The coherence exhibits angular dependence because the electrons are expected to spread out more along the direction of laser polarization than they do along the direction perpendicular to it.

2.2 Measured Nonlinear Thomson Scattering with Helium and Argon

We measured nonlinear Thomson scattering for fundamental, second harmonic, and third harmonic using argon to donate free electrons. We compared the results with those obtained using helium. The data collected is shown in Fig. 2.6.

The theoretical calculation shown in the figure uses the instantaneous ionization model. This model gives more coherence signal than the more realistic ADK model. I performed these calculations prior to the ones performed by our colleague Prof. Nuno Sá who made them again with the ADK model.

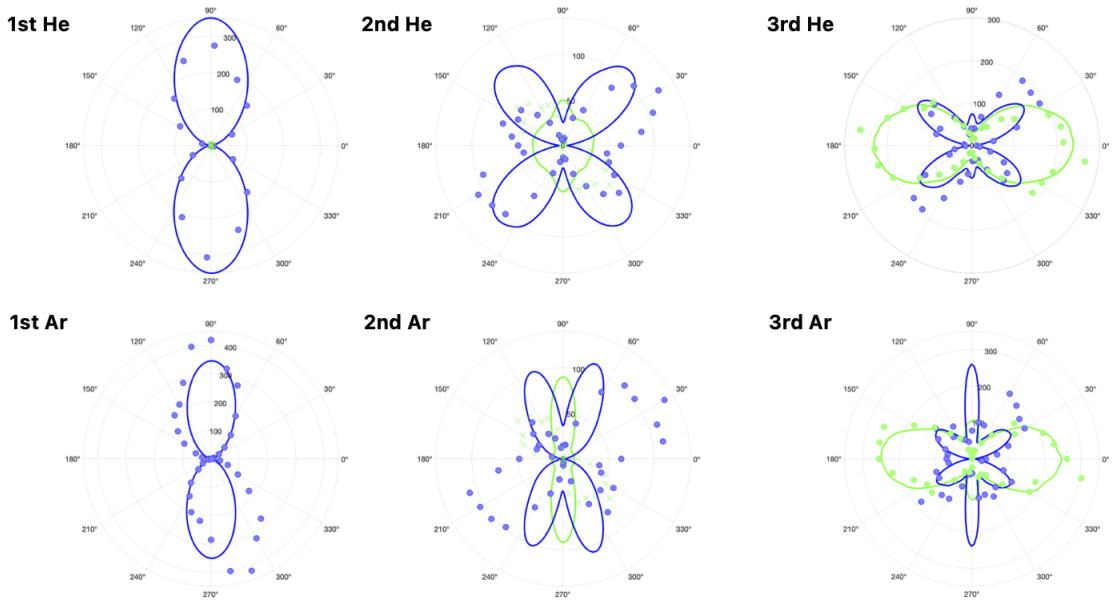

Figure 2.6 Radiation emission pattern (azimuthal and longitudinal polarization) for first, second and third harmonics of helium(top row)and argon(bottom row)

Unexpectedly, we did not see any differences in the angular pattern of nonlinear Thomson scattering between the two gasses. In particular, the predicted elongated pattern for longitudinal polarization was not evident.

We suspect that a prepulse or multiple prepulses generated in the laser system (i.e., weak pulses arriving arriving to the experiment before the main pulse) may have pre ionized the gas to some degree at much earlier times than expected. In this case, the relative positions of the electrons could become completely decorrelated by the time the main laser pulse arrived. In other words, prepulses could have completely disrupted the experiment.

2.3 Reducing Laser Prepulses

Prepulses are a well known and common problem in high-power laser systems if not specifically addressed. The most common way to reduce prepulses is through frequency doubling in a nonlinear crystal. The process suffers from inefficiency (10% - 50%), but more importantly, the doubling of the frequency requires a quadrupling of the intensity to achieve the same relativistic regime for nonlinear Thomson scattering. Hence, frequency doubling in not an option for us.

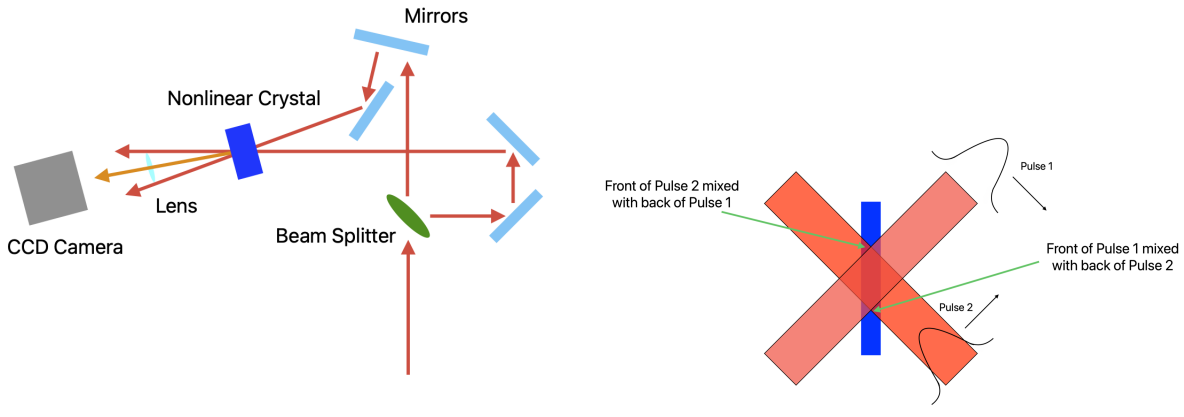

Figure 2.7 Setup for an autocorrelation measurement.

We investigated the possibility of prepulses in our laser system using autocorrelation. A schematic of our autoccorrelation measurement is shown in Fig. 2.7. In this technique, the laser beam is split into two beams and mixed in a thin nonlinear crystal with a crossing angle of a few degrees. The signal that arises from a mixing of the two pulses is imaged onto a camera so that the mathematical temporal autocorrelation of the pulse appears as a spatial image on the camera. The width of the image can be calibrated to time units by temporarily delaying one pulse relative to the other by known amounts and observed how far the image of the mixing region shifts laterally.

Through autocorrelation, we can infer the temporal structure of the pulse. The autocorrelation setup consists of a beamsplitter that produces two identical pulses in separate beam paths. The pulses travel similar distances and mix in a nonlinear crystal and produce a second harmonic beam. The two pulses are unfocused, so they are like two thin pancakes of light that intersect along a narrow line. The emerging second-harmonic light is imaged onto a camera. The width of the line on a camera shows the duration of the pulses, or rather a mathematical correlation between them ("auto" since the pulses are identical). For our setup, we found that each pixel in the image corresponded to 1.3 fs of the autocorrelation function. When our compression gratings are optimally adjusted, the autocorrelation measurements indicated a pulse duration of 40 to 45 fs.

Figure 2.8 shows two intense side lobes in the autocorrelation, which we measured to be about 6.7% of the center peak. Unfortunately, the correlation integral of a function with itself is always symmetric. When we see side lobes in the autocorrelation function, they can be due either to a prepulse, a postpulse, or a combination of the two. In an effort to reduce the side lobes, we made adjustments to the laser system.

We determined experimentally that the worrisome feature in the autocorrelation arises mainly from our first of three Ti:sapphire amplifiers in our laser system. We switched to a Brewster cut Ti:Sapphire crystal and reconfigured the amplifier layout to tighten the beam angles in the layout. This had the effect of significantly reducing the side lobes in the autocorrelation.

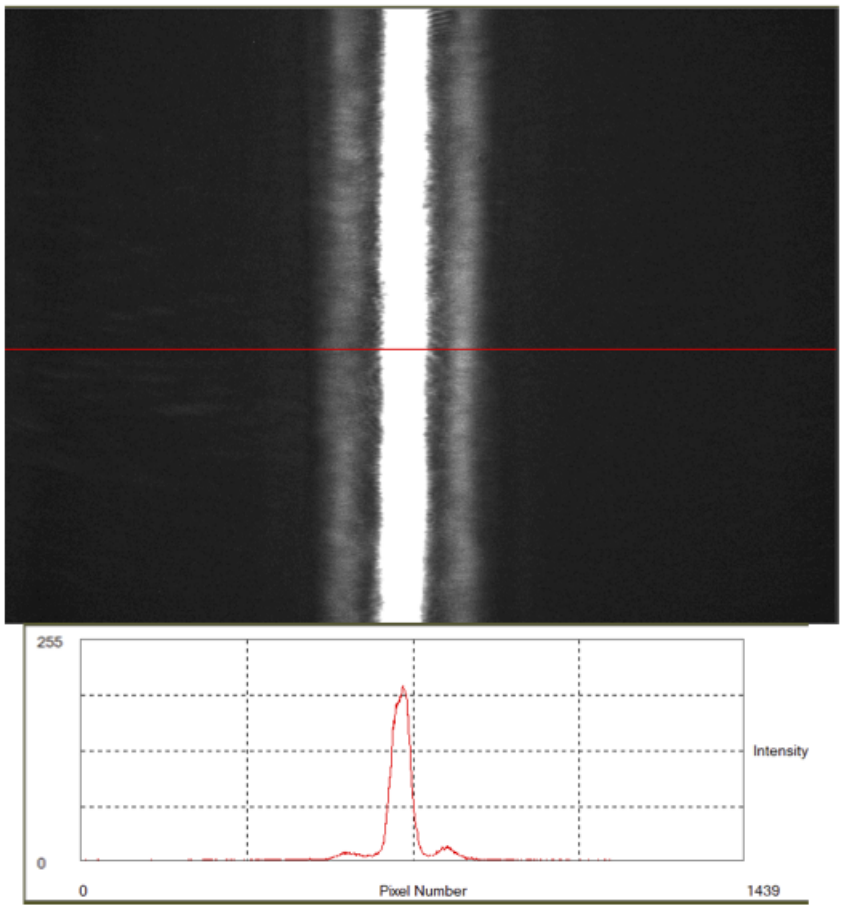

Figure 2.8 Autocorrelation measurement and lineout. The exposure of the image was intentionally saturated in the center to better show the side lobes. The lineout was taken from an image that was not saturated.

Figure 2.9 shows the schematic setup for the redesigned first amplification stage. The beam passes through the Ti:Sapphire crystal for a total of eight passes, utilizing ten mirrors. There are four small mirrors and one large mirror on each end of the amplifier. The beam diameter is controlled by several 1-m-focal-length lenses throughout the amplifier. The beam reflects off of a small mirror and subsequently a large mirror before each pass through the laser crystal. After eight passes, we have a total gain of $G = 10^7$; it would be $G = 10^8$ if not for saturation on the final two passes. The energy increases from 0.1 nJ to 10 mJ. The saturation helps reduced shot-to-shot energy fluctuations.

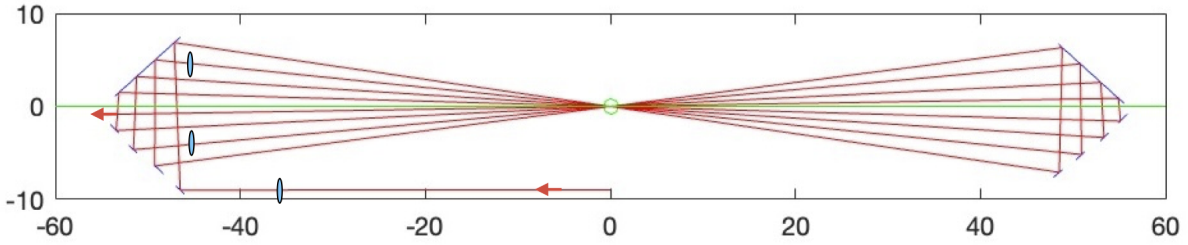

Figure 2.9 Schematic of first amplifier stage. The green lines represent the pump laser (directed into the Ti:sapphire crystal from both sides) while the red lines represent the path of the 800 nm laser pulse.

Figure 2.10 shows the autocorrelation after the upgrade to the first amplifier stage. The side lobes in the autocorrelation were reduced to about 1%. Since the peak of the main pulse in our experiment reaches an intensity of 10^{18} W/cm^2, the prepulses occur at an intensity of 10^{16} W/cm^2, which is still well above the ionization threshold for both electrons in helium and for the majority of electrons in argon.

Using the autocorrelator setup, we also investigated the possibility of prepulses at times far in advance of the main pulse. Figure 2.10 shows a possible prepulse that occurs well away from the main pulse in time. We could see several of these weak pulses away from the main peak. We determined that some of them were artifacts in the autocorrelator setup, for example, arising from a weak reflection from the wrong side of the beamsplitter, deduced by it not being symmetric and by it shifting when switching the thickness of the beam splitter.

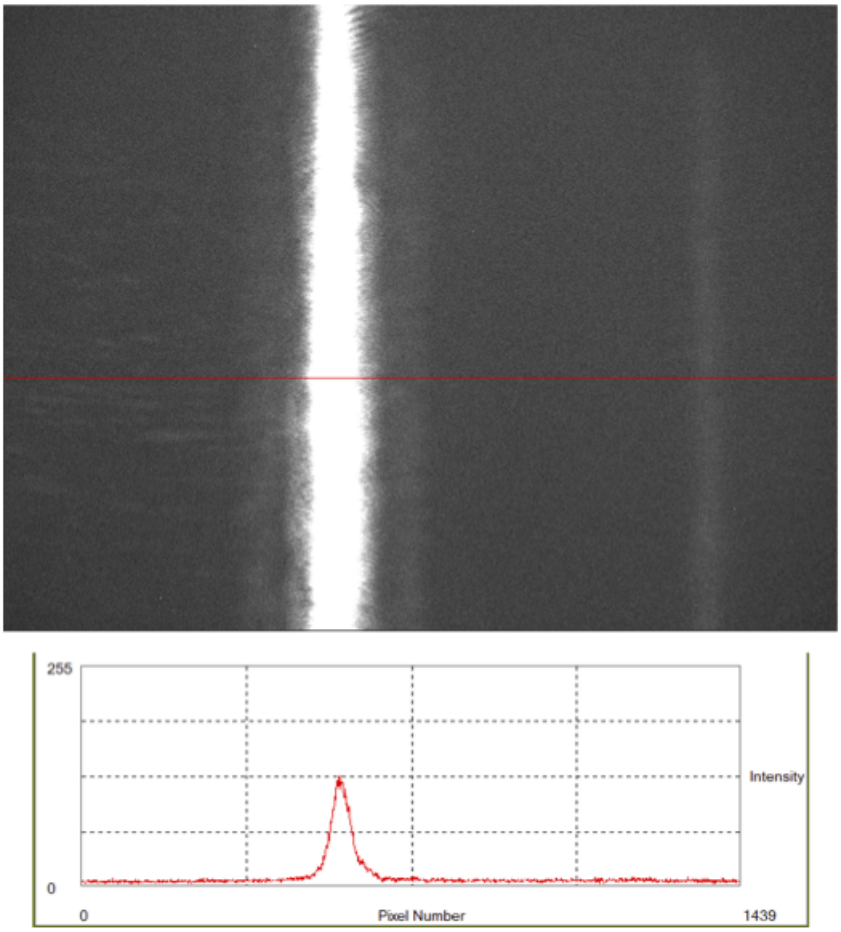

Figure 2.10 Autocorrelation measurement and lineout. The exposure of the image was intentionally saturated in the center to better show the side lobes. The lineout was taken from an image that was not saturated.

2.4 First Attempt at Temporal Pulse Cleaning

In an attempt to clean prepulses from the laser pulse, we created a strong temperature gradient in helium. The ends of two 1-cm-wide copper rods were held 1-mm apart to create a narrow gap. One rod was cooled with liquid nitrogen, and the other was heated to about 280 °C. A schematic of the setup is shown in Fig. 2.11, and pictures of the experiment are shown in Fig. 2.12.

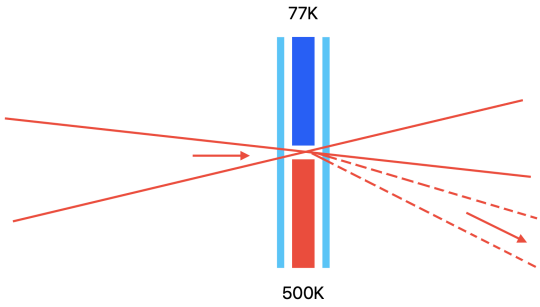

Figure 2.11 Experimental setup for pulse cleaning. A copper rod is cooled and another is heated. Helium fills a small gap between them. This is a separate and larger focal spot in advance of subsequent optic that refocuses the beam to a tight spot for experiments with nonlinear Thomson scattering.

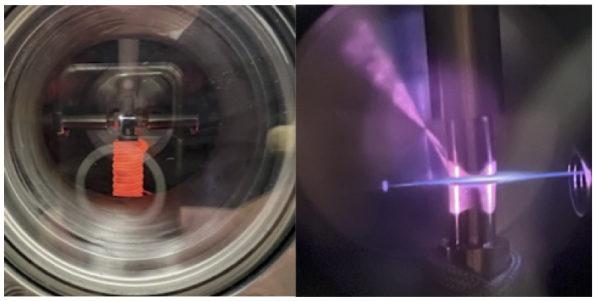

Figure 2.12 Experimental setup showing our laser pulse ionizing helium between two molybdenum foils. A copper rod above is cooled with liquid nitrogen, and a coper rod beneath is wrapped with a heating coil.

When filled with helium, the gas density was expected to vary by roughly a factor of five across the 1 mm gap, according to the ideal gas law. The laser, focused to a diameter of about 50 µm, was sent through the gap such that it interacted with the helium over a distance of about 1 cm. The laser was used to burn a hole through a 160 µm-thick molybdenum foil at the beginning and end of the gas cell. The foil separated the 1 cm gas cell from surrounding vacuum maintained by differential pumping.

When the helium is ionized by the main laser pulse (with peak intensity 10^{16} W/cm^2), the the refractive index of the resulting plasma deviates from unity by about 40 times that of the original helium. We expect that the plasma to inherit the density gradient of the gas. This would create and a mirage effect that would deflect the main laser pulse into a new direction once the plasma formed [16].

The result of this effort was disappointing. To get sufficient beam deflection, we required 100 Torr of helium, but unfortunately, the laser beam was also unacceptably distorted when ionizing so many atoms in the laser path.

Since the laser beam width is about 20 times narrower than the 1 mm gap between the ends of the two copper rods, the difference in gas density between one side of the beam to the other was only about 5% of the available difference across the whole gap. In summary, to achieve the desired density gradient, it was necessary to interact the laser with too high of gas density. A related but different scheme for cleaning the laser pulse is outlined in chapter 4.

Chapter 3

Distortions in Angular Emission Patterns

3.1 Measured Asymmetries in Angular Emission Patterns

While measuring nonlinear Thomson scattering, the emission pattern frequently displayed distortions relative to the calculated models, while at other times the pattern is symmetric. Figure 3.1 compares data that displays expected symmetry (left) with data that displays angular distortions that arise under nominally the same laser conditions. We initially postulated that that uncontrolled distortions in the laser focus lead to the asymmetries that we sometimes observe in our measurements. If this were indeed the case, then our nonlinear Thomson scattering measurements provide a possible diagnostic for focal imperfections. We set out to explore this possibility both theoretically and experimentally.

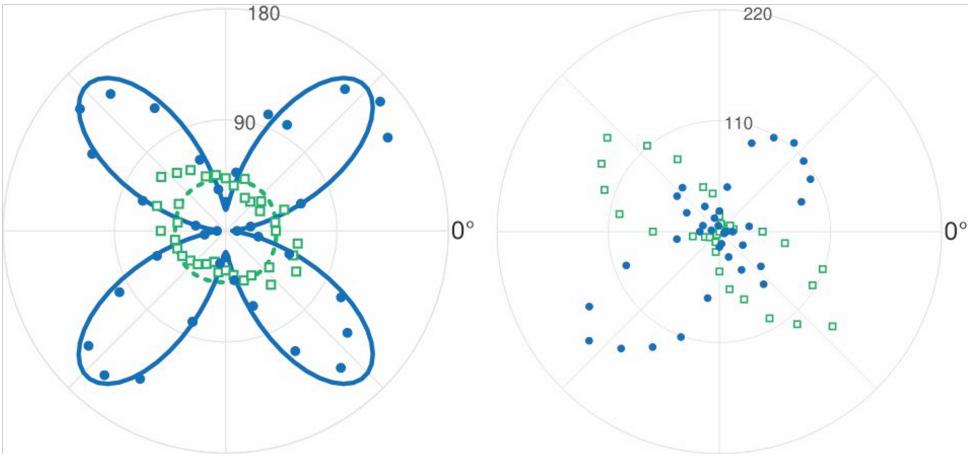

Figure 3.1 Measured angular distribution of 2nd harmonic nonlinear Thomson scattering in a plane perpendicular to laser propagation. The left panel shows scattering from a particular laser focus together with theoretical prediction. The right panel shows scattering from a less-than-ideal laser focus with similar intensity. Blue indicates photons polarized in the scattering plane while green indicates scattered photons polarized perpendicular to that plane.

3.2 Simulation of Focal Defects

To better understand emission patterns corresponding to electron trajectories, we simulated the electrons leaving from different quadrants of the focus and their corresponding radiation. Keep in mind that during the laser pulse, electrons tend to be expelled from the focus radially even as the are also pushed forward by the pulse. This expulsion of the electrons tends to be radially symmetric except for the aforementioned initial velocity associated with the phase of the field at the moment of ionization – a minor effect on how electrons exit the focus. The radial components of a large number of possible trajectories, starting from random positions in the focal plane, are shown in the left frame of Fig. 3.2. The emission pattern from individual trajectories is strongly dependent on which direction the electron exits the focus, which in turn depends on the initial position of the electron. Nevertheless, the average emission pattern from many electrons exiting the focus in all directions tends to average to a pattern similar to that from a single electron experiencing a plane-wave pulse.

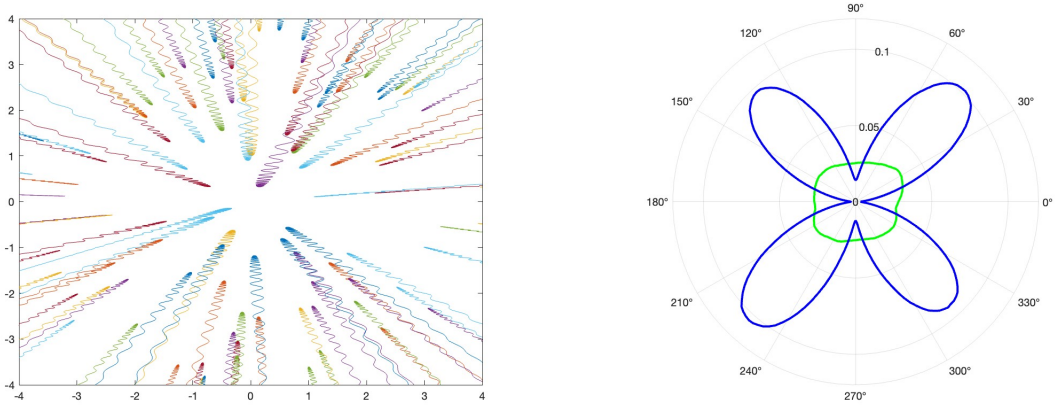

Figure 3.2 Simulated electron trajectories starting from random positions in the focal plane of an ideal (round) focus. The cumulative emission pattern is shown on the right. The radial components of the trajectories are projected onto a plane perpendicular to the laser focus.

Figure 3.3 shows four typical individual electron trajectories leaving the focus in four different directions together with their corresponding *individual* emission patterns. The emission patterns are severely distorted. The usual clover pattern of the azimuthal polarization in each case has two big wings and two small wings. This is similar to the kinds of distortions that we sometimes see in experiments. We speculated that distortions in our laser focus could cause electrons to leave the laser focus along preferred directions and that this could distort angular emission patterns even when the emission from many electrons is averaged.

We simulated a group of 100 electrons leaving the focus along two directions only, as shown in Fig. 3.4. Unsurprisingly, the corresponding emission pattern has two big leaves and two small leaves of the clover, similar to the kinds of distortions we have seen experimentally.

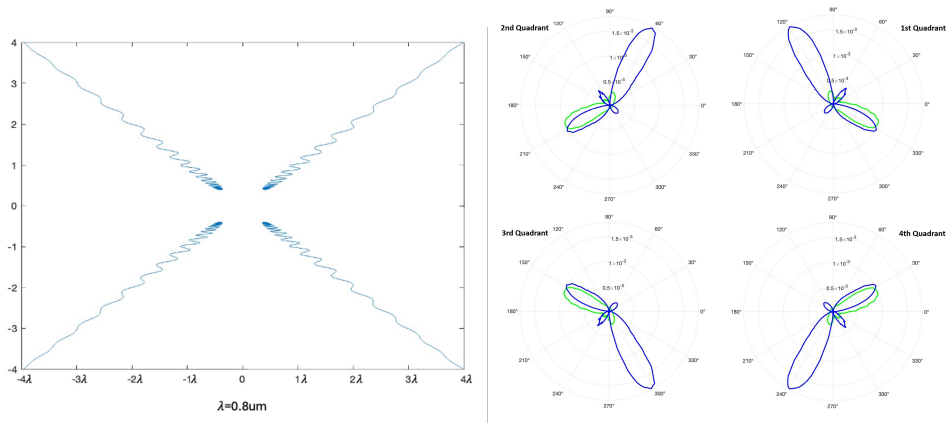

Figure 3.3 Radial trajectories of four electron initial positions near the focal center. Equatorial radiation patterns for the four initial electron positions.

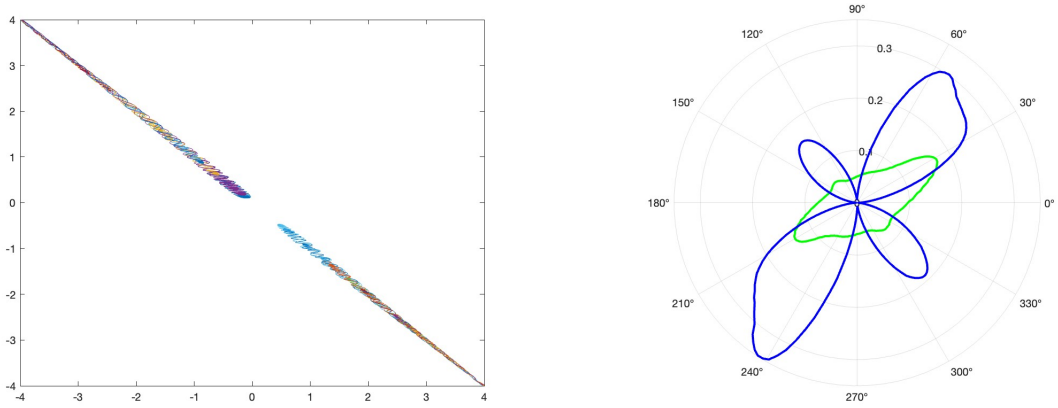

Figure 3.4 1000 electrons leaving the distorted focus in two directions and its corresponding emission pattern.

Next, we simulated the emission pattern for 100 electrons randomly distributed throughout the focal plane of an oval shaped focus with an aspect ratio of 2:1 and with its long axis running from the second quadrant to the fourth. In this case, the emission pattern is only mildly distorted. While the simulations involving electrons that leave the focus along a single dimension are suggestive, this more realistic simulation involving merely a preference in direction for electrons leaving the focus fails to explain the asymmetries in our angular emission patterns. We must look further for an explanation.

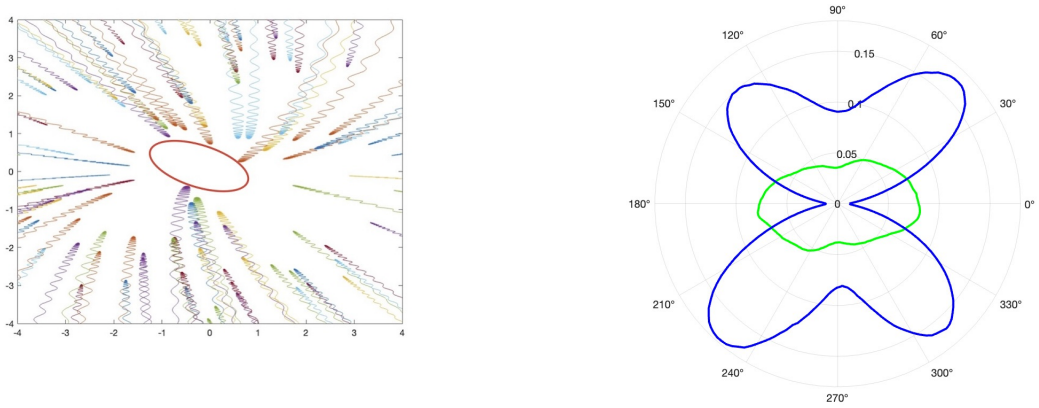

Figure 3.5 Simulated electron trajectories leaving an oval shaped focus and its corresponding emission pattern.

3.3 Laser Characterization and Alignment

In an effort to determine the cause of asymmetries in our angular emission patterns, we systematically characterized our laser focus. We examined the possible presence of spatial chirp using a spectrometer. We focused the laser, after the compression gratings, using a $f = 2.5$ m lens. This produced a focus several hundred μm wide. We sampled the light in the focus using a 100 μm fiber on a translation stage connected to the spectrometer. We scanned through the focus horizontally and vertically and could notice the spectrum varying with position. Spatial chirp occurs when the compressions gratings are misaligned. We were able to tune out the spatial chirp through subtle adjustments to the tilt and shear alignment of the compression gratings. We achieved a uniform and full spectrum throughout the laser focus.

We also eliminated astigmatism in the beam by placing a camera directly in the focus after strongly attenuating the energy with filters. We moved the camera slightly upstream and downstream of the focus using a translation stage. We tuned out the astigmatism of the beam by adjusting the vertical and horizontal knobs on the laser focusing mirror.

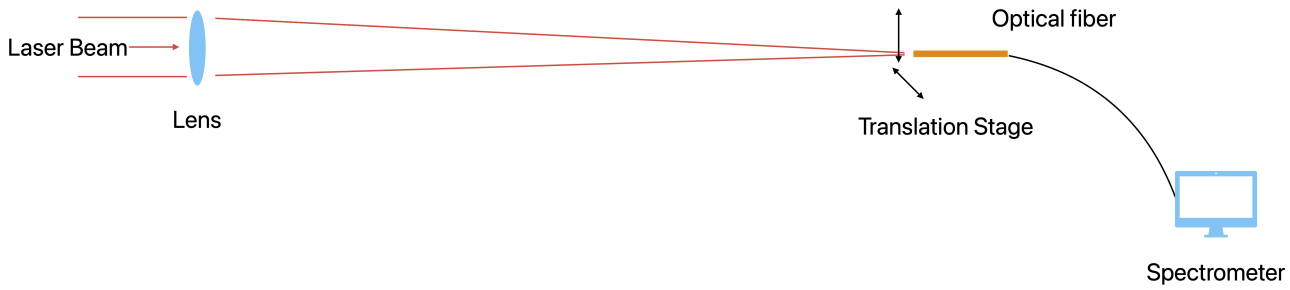

Figure 3.6 Experimental setup to measure spatial chirp in focused laser. A fiber couples to a spectrometer samples portions of a large laser focus.

The focus was so tight that it illuminated just one pixel (3.2 µm) on the CCD camera. We also imaged the focus using a 10x microscope objective to further analyze the focal shape of the beam. As shown in Fig. 3.7, we were able to make the focal shape quite symmetric. We could achieve a similar focus both with an off-axis parabola and with an on-axis elliptical mirror.

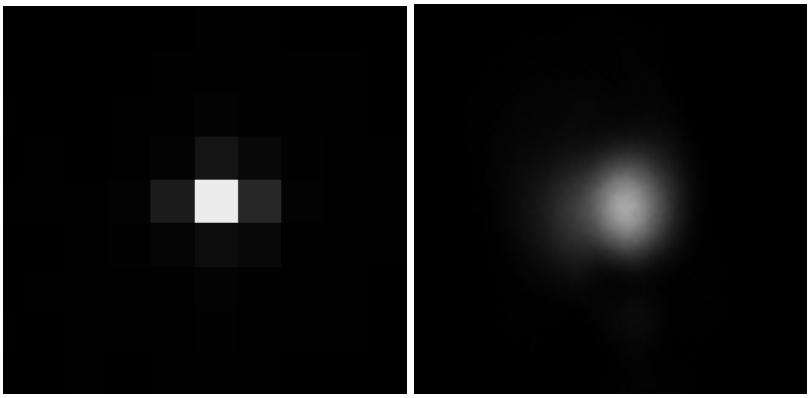

Figure 3.7 Laser focus captured on a camera, directly (left) and through 10x microscope objective (right).

3.4 Detector Alignment

For detecting scattered photons from the interaction region, we have used both a mirror based collection system and a lens based collection system. Both appear to perform equally well. The goal is to image the focus onto a 105 µm fiber which connects to a single-photon detector. For alignment purposes, we temporarily sent an ultraviolet laser beam backwards through the fiber to aid in alignment of photon collection system. We temporarily placed a small needle at the center of the rotation stage and made sure the ultraviolet laser and the main laser pulse hit at the tip of the needle at the same spot. After this initial alignment, we disconnected from the ultraviolet laser and temporarily connected the fiber to a spectrometer. We used motorized translation stages beneath the collection system to further align collection system to the laser focus. With the chamber open to atmospheric pressure, we aligned on a 500 nm emission line generated from nitrogen in a spark at the laser focus.

3.5 Off-Axis Parabolic Mirror vs. Elliptical Mirror

We can use either and off-axis parabolic mirror or an on-axis elliptical mirror to focus our laser pulse to a 4 µm spot. We analyzed the focus of both optics and compared their performance when generating nonlinear Thomson scattering. We saw no appreciable difference between them and conclude that the focusing optic is not responsible for asymmetries in the angular emission patterns.

We were concerned that the laser polarization (rotated by a wave plate during the experiment) might be modified by reflection from the off-axis parabola. Measurements of the polarization, while strongly attenuating the laser energy, showed less than 1% variation in its polarization after reflection from the parabola. On the other hand, the on-axis elliptical mirror is not expected to modify the polarization provided by the wave plate.

To further confirm that the focusing optic is not responsible for asymmetries in our emission data, we rotated the elliptical mirror 90 degrees. We found the distorted angular emission pattern did not rotate with the mirror.

3.6 Signal Detection System and Photon Counter

At the end of the fiber optic, we can detect second harmonic photons with either an avalanche photodiode or a photomultiplier tube. The distortions in our angular emission patterns were not affected by which detector was used. Neither were they affected by the use of different optical fibers or placing additional optical shielding around the fiber. Moreover, the use of the aforementioned reflective collection system or lens collection system, had no effect on the asymmetries in the data.

3.7 Laser Beam Rotation

After carefully eliminating errors in our laser focus, we performed a simple but powerful test to see if the distortions in the angular emission patterns could still be due to something intrinsic to our laser system. First, we inserted an extra (flat) mirror in the beam just before our experiment. This has the effect of inverting left and right sides of the laser beam. However, the left and right sides of the angular distortion did not flip. We also inserted two additional mirrors to create a periscope that rotated the beam by 90 degrees. (The polarization had to be rotate back to the original state using the wave plate.) Again, no change was seen to the asymmetric distortions in the data. If the asymmetry were inherent to the laser beam, these two tests should have revealed it. The results of these tests require the source of the distortion to occur after the point of beam rotation, and there remain only two elements prior to the interaction region: the wave plate and the focusing mirror.

3.8 Wave Plate

We use a half wave plate to rotate the laser polarization, just before the focusing mirror of our experiment. We temporarily installed a polarizer after the wave plate to check the wave-plate performance. A wave plate is a crystal with a fast axis and slow axis cut parallel to the crystal surface. When interacting with a plane-wave at the design wavelength, the half wave plate introduces a half-wavelength delay to the wave front of the polarization aligned with the slow axis, which causes the polarization axis to rotate.

We verified that linearly polarized light remains linear, judged by extinguishing the light with the temporary polarizer. Only about 0.3% of the light leaks through the polarizer when rotated to extinguish the beam. This implies an aspect ratio for possible ellipticity of the field be less than 1:10. Our simulations of nonlinear Thomson scattering suggests that emission is virtually the same for this amount of ellipticity and for linear polarization.

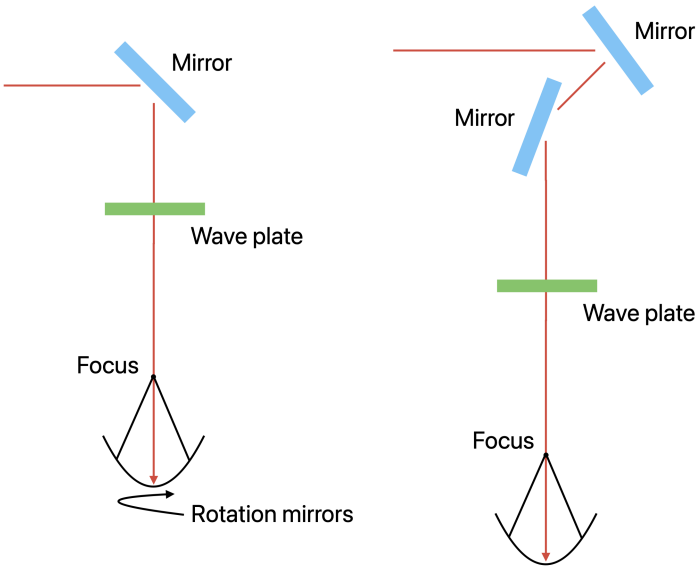

Figure 3.8 Wave plate and focusing mirror. As of test, the focusing mirror was rotated (left) and the laser beam was rotated (right).

Since the polarization-contrast measurement is necessarily made at low intensity, there remains the question of whether the wave plate performs differently at high intensity, where we operate just shy of the damage threshold for the crystal. We measured nonlinear Thomson scattering at two different laser intensities (about a factor of 2 between them), and we saw no difference in the asymmetries in the angular emission patterns. This tends to dismiss the possibility of a nonlinear effect in the wave plate. Nevertheless, the previously described tests of rotating the laser beam prior to the wave plate and of rotating the focusing optic after the wave plate, with no effect on the measured emission, tends to implicate the wave plate as the source of asymmetry through some yet-to-be-discovered cause.

Chapter 4

Outlook

If accepted, I plan to continue with my research at BYU and transition to the doctoral program in the Department of Physics and Astronomy. This chapter outlines proposed research to solve experimental challenges outlined in the preceding chapters to accomplish experiments that we are presently working on. In additional, I propose possible experiments to measure, for the first time, fourth harmonic and possibly fifth harmonic of nonlinear Thomson scattering. Also, I propose to examine nonlinear Thomson scattering in colliding intense laser pulses, both theoretically and experimentally. Alltogether, these investigations could lead to a number journal articles.

4.1 Laser Pulse Temporal Cleaning

We have an idea for increasing the temporal contrast of our laser pulse. This is related to our previous effort to create a mirage effect triggered by ionization, described in Sect. 2.4. Rather than try to deflect our laser pulse using a side-to-side temperature gradient of gas before the pulse ionizes it, we will rely on a radial density gradient induced by the laser pulse itself in an initially uniform gas distribution. In either case, weak prepulses should traverse the gas unaffected if the fail to ion the gas.

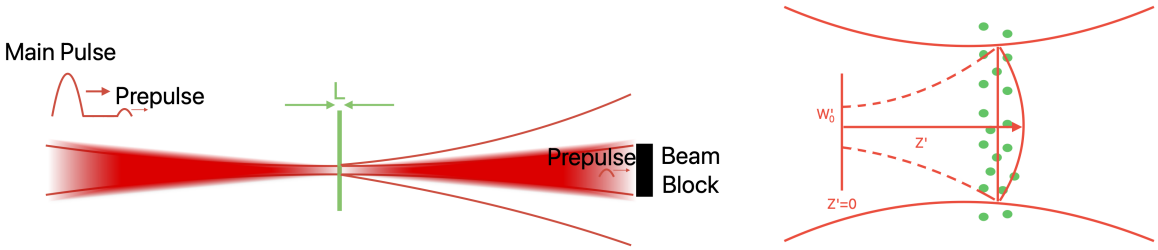

Figure 4.1 Concept for cleaning prepulses from the laser beam. The laser ionizes a low-density thin cell of argon to create a radial plasma profile. The center of the wider emerging beam is blocked, and a prepulse-free portion of the beam passes around the outside. The right figure shows how the plasma changes advances the on-axis wavefront.

In the radial-gradient approach, we again rely on a separate pre focus that is later refocused to a smaller spot for experiments. The pulse-cleaning pre focus should be sufficiently large to have a peak intensity of about 10^{16} W/cm^2 if, say, argon is used, which can become ionized up to six times (when surpassing intensities 0.25, 0.58, 1.2, 3.2, 5.1 and 7.6 $\times 10^{15}$ W/cm^2).

An overview of the experimental approach is shown in Fig. 4.1. If the pulse focuses with beam waist w_0 into a uniform gas cell with length $L < z_0$, the resulting plasma in the center of the focus will advance the wavefront relative to the wavefront at larger radii. This will cause the emerging beam to be wider (i.e. have a significantly smaller f-number) as it emerges from the focus. If the emerging beam is, say, three times wider, the center can be blocked to eliminate prepulses that does not undergo the beam widening. A large fraction of the original pulse energy can then be captured around the outside and directed to an experiment.

The widened beam will emerge from the plasma as though from a virtual focus. To accomplish a factor of three in width, the emerging beam would need to exit the gas cell at new position z' (with local beam radius w_0) following the virtual focus with waist $w_0' = w_0/3$. This means

$$w'\left(z'\right) = w_0'\sqrt{1+z'^2/z_0'^2} = w_0 \quad \text{where} \quad w_0' = w_0/3 \quad \text{and} \quad z_0' = \frac{\pi w_0'^2}{\lambda} = \frac{\pi w_0^2}{9\lambda} \tag{4.1}$$

The distance from the virtual focus z' can be solved:

$$w_0 = w_0/3\sqrt{1+\frac{z'^2}{\left(\frac{\pi w_0^2}{9\lambda}\right)^2}} \;\Rightarrow\; z' = \frac{2\sqrt{2}\pi w_0^2}{9\lambda} \tag{4.2}$$

Moreover, the radius of curvature of the wavefront for the emerging beam would be

$$R\left(z'\right) = z' + z_0'^2/z' = \frac{2\sqrt{2}\pi w_0^2}{9\lambda} + \frac{\left(\frac{\pi w_0^2}{9\lambda}\right)^2}{\frac{2\sqrt{2}\pi w_0^2}{9\lambda}} = \frac{\pi}{9}\left(2\sqrt{2}+\frac{1}{2\sqrt{2}}\right)\frac{w_0^2}{\lambda} = 1.11\frac{w_0^2}{\lambda} \tag{4.3}$$

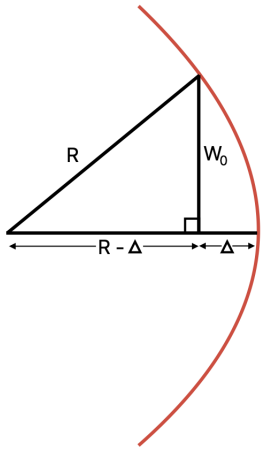

Figure 4.2 Geometry of wavefront advancement

Finally, by referring to Fig. 4.2, we can estimate how much the wavefront would need to advance in the center relative to radius w_0 —call the advance Δ —to produce this curvature.

$$(R-\Delta)^2 + w_0^2 = R^2 \;\Rightarrow\; \Delta \approx \frac{w_0^2}{2R} = 0.45\lambda \tag{4.4}$$

We just need a difference in optical path length between the center of the ionized region and the outside to be Δ. Since the index of refraction for a low-density plasma is

$$n \approx 1 - \frac{Ne^2}{8\pi^2\varepsilon_0 m_e c^2}\lambda^2 \quad \text{where} \quad N = \frac{6P}{k_B T}\,, \tag{4.5}$$

assuming a maximum of six electrons per atom, we need

$$\frac{6Pe^2\lambda^2}{8\pi^2 k_B T \varepsilon_0 m_e c^2} L = \Delta = 0.45\lambda \tag{4.6}$$

This dictates the product of thickness and pressure needed for the gas cell:

$$\begin{aligned} PL &= 0.45 \frac{8\pi^2 k_B T \varepsilon_0 m_e c^2}{6e^2\lambda} \\ &= 0.45 \frac{8\pi^2 \left(1.38\times10^{-23}\,\frac{\mathrm{J}}{\mathrm{K}}\right)(300K)\left(8.85\times10^{-12}\,\frac{\mathrm{C}^2}{\mathrm{Nm}^2}\right)\left(9.11\times10^{-31}\mathrm{kg}\right)\left(3\times10^{8}\,\frac{\mathrm{m}}{\mathrm{s}}\right)^2}{6\left(1.60\times10^{-19}\mathrm{C}\right)^2\left(8\times10^{-7}\mathrm{m}\right)} \\ &\quad \times \left(\frac{760\text{ Torr}}{1.013\times10^5\text{ N/m}^2}\right)\left(\frac{1000\text{ mm}}{1\text{ m}}\right) \\ \Rightarrow \quad PL &= 6.5\text{ Torr}\cdot\text{mm} \end{aligned} \tag{4.7}$$

This is easily achievable, for example, with a 3-mm gas cell and 2 Torr of gas. Moreover, our laser pulse can reach 10^{16} W/cm^2 with a focal radius of 30 µm, which gives a Rayleigh range of 3.5 mm, which is plenty long.

If successful, this temporal pulse-cleaning scheme could in itself produce a publication, in addition to enabling our electron coherence experiment, which could produce another publication.

4.2 Rotating the Detector around Focus Instead of Rotating the Polarization

The interaction region in our nonlinear-Thomson-scattering experiments is on the scale of 10 µm across. The imaging system that collects scattered photons images this small region onto the end of an optical fiber with a similar dimension. Alignment of the imaging system requires precision on this same spatial scale. For this reason, it is much easier to rotate the linear laser polarization rather than the detector around the focus.

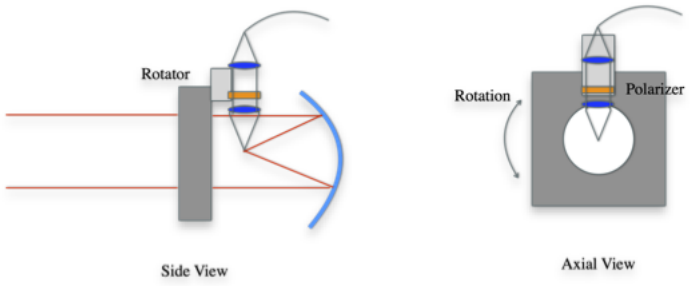

Figure 4.3 Setup setup for rotating the light-collection system.

The laser polarization is rotated with a half wave plate before the focusing mirror. However, as described previously, we suspect that the wave plate may not be performing as expected, and so we have taken on the ambitious project of reconfiguring the experimental setup to remove the wave plate and instead rotate the detector around the focal plane. The Detector must remain precisely aligned to the laser focus as it rotates around the focus at a distance of about 5 cm away.

A schematic of the proposed setup is shown in Fig. 4.3. To align, we first center a needle on the axis of a rotation stage. This is confirmed by rotating the stage while viewing the needle close up with a camera. If centered, the needed should not wobble as the stage rotates. We next temporarily send light backwards through the fiber optic and the imaging system, which focuses that light to a small spot where the intense laser pulses should later intersect. The aiming of the imaging system is then adjusted to place the spot (from the injected backwards-going light) onto the needle. The needle is then removed and the setup placed in the experimental chamber. The backwards going light is also no longer needed, and the fiber is connected to the photon counter or other light sensor used during preliminary alignment to the laser pulse.

The xyz translators below the whole setup are then adjusted until light from the focused laser pulse makes it through the photon collection system and into the fiber. The alignment is then optimized to maximize detection of nonlinear Thomson scattering.

It is anticipated that rotation of the detector around the focus will result in slight misalignment of the photon collection system. Of course, this could produce significant distortions to the angular profile of the signal. Therefore, it will be critical to carefully re optimize the signal through spatial alignments as the rotation angle varies.

If successful, this approach will allow us to remove the half wave plate from our setup and thereby determine its effect on the experiment, since it has been implicated as a source of experimental distortion. This should help us to better understand the wave plate's performance at high intensity and ultrashort duration. This potentially could lead to a publication about the wave plate behavior, but more importantly, it will allow us to characterize the response of nonlinear Thomson scattering to focal aberrations and laser spatial chirp without unknown confounding influences – also a future publication.

4.3 Other Experiments with Nonlinear Thomson Scattering

Our all-reflective collection system for nonlinear Thomson scattering is capable of gathering 4th- and 5th-order harmonics from nonlinear Thomson scattering, in addition to 1st-, 2nd-, and 3rd-order harmonics that we have previously detected. However, the fiber optic will not transmit 200 nm (4th) or 160 nm (5th) light. To detect these wavelengths, we would need to place the photo multiplier tube inside the chamber, directly coupled to the photon collection system. In addition, we would need to find suitable bandpass filters to measure the light in these wavelength ranges. Such filters exist for the fourth harmonic, namely, and argon-gap filter peaked at 206 nm with 12 nm full-width

at half maximum transmission. Otherwise we could consider using a UV prism to distinguish wavelengths. Measuring one or two new harmonic orders of nonlinear Thomson scattering is a worthy endeavor and could result in a journal publication. It could also be a challenge since the efficiency of harmonic production goes down with each order.

Another experiment that we would like to try in the future is measurement of nonlinear Thomson scattering from free electrons in crossed laser beams. Measurements from counter-propagating pulses would also be interesting (a standing wave), but electrons might not experience sufficient red shift, which helps distinguish nonlinear Thomson scattering from other background noise photons. Moreover, in a counter-propagating configuration, the residual laser light would be directed back into the amplifier, which could damage optics.

Earlier in his career, Prof. Peatross' group performed experiment at lower intensities in both counter-propagating and orthogonally crossed beams [17], so our group possesses experience in aligning laser pulses in this way. Depending on the relative polarization of the crossing laser pulses, the trajectory of free electrons at high intensity can be quite different than the figure-8 for linearly polarized light. This may lead to interesting differences in angular radiation patterns. This could be the basis of a journal publication.

4.4 Summary

In this thesis, I have described our experimental results measuring fundamental, second, and third harmonics from nonlinear Thomson scattering over the full emission sphere for a linearly polarized tightly focused 40-fs laser pulse. These results demonstrated unambiguously for the first time the figure-8 motion that a free electron follows in a relativistic laser field. It also shows the direction that the electron takes around the "racetrack."

We simulated coherence effects between multiple electrons freed from the same atom as they radiate nonlinear Thomson scattering later during the laser pulse. Our preliminary measurements did not exhibit these effects, but we identified the presence of pre pulses in our laser system that could disrupt the coherence between electrons. We propose a scheme for cleaning the laser pulse using self-induced angular broadening of the laser beam that emerges from a pre focus where the main part of the pulse generates a radially varying plasma.

We investigated distortions in angular patterns of nonlinear Thomson scattering. To better understand these distortions, we eliminated the possibility that they arose from intrinsic asymmetries in our post-compression laser beam or from the focusing mirror. That leaves just the wave plate used to rotate laser polarization as the likely culprit. We are making a setup to rotate the detector around the laser focus so that the wave plate can be eliminated. That should conclusively demonstrate whether the wave plate is responsible for the observed distortions. If so, it will be interesting to determine the physical mechanism responsible.

We have also proposed additional experiments on nonlinear Thomson scattering, namely measuring harmonics of higher order and colliding laser pulses to produce interesting electron trajectories in the intense laser field besides the figure-8.

Bibliography

[1] J. J. Thomson, *Conduction of Electricity through Gases* (Cambridge University Press, 1906).

[2] J. D. Jackson, *Classical Electrodynamics* (Wiley; 3rd edition, 1998).

[3] D. J. Griffths, *Introduction to Electrodynamics*, 4th ed. (Pearson, 2017).

[4] L. D. Landau and E. M. Lifshitz, *The Classical Theory of Fields* (1951).

[5] Vachaspati, "Harmonics in the Scattering of Light by Free Electrons," Phys. Rev. **128,** 664–666 (1962).

[6] J. H. Eberly and A. Sleeper, "Trajectory and Mass Shift of a Classical Electron in a Radiation Pulse," Phys. Rev. **176,** 1570–1573 (1968).

[7] E. S. Sarachik and G. T. Schappert, "Classical Theory of the Scattering of Intense Laser Radiation by Free Electrons," Phys. Rev. D **1,** 2738–2753 (1970).

[8] B. Pratt, N. Atkinson, D. Hodge, M. Romero, C. Schulzke, Y. Sun, M. Ware, and J. Peatross, "Experimental confirmation of electron figure-8 motion in a strong laser field," Phys. Rev. A **103,** L031102 (2021).

[9] M. Ware, E. Cunningham, C. Coburn, and J. Peatross, "Measured photoemission from electron wave packets in a strong laser field," Optics Letters **41,** 689–692 (2016).

[10] W. Erikson and S. Singh, "Polarization properties of Maxwell-Gaussian laser beams," Phys. Rev. E **49,** 5778–5786 (1994).

[11] S. Chen, A. Maksimchuk, and D. Umstadter, "Experimental observation of relativistic nonlinear Thomson scattering," Nature **396,** 653–655 (1998).

[12] C. Fruhling, J. Wang, D. Umstadter, C. Schulzke, M. Romero, M. Ware, and J. Peatross, "Experimental observation of polarization-resolved nonlinear Thomson scattering of elliptically polarized light," Phys. Rev. A **104,** 053519 (2021).

[13] M. Romero, L. Robins, A. Stevens, N. Sa, Y. Sun, M. Ware, and J. Peatross, "Nonlinear Thomson scattering: velocity asymmetry inherent in electron figure-8 motion," Optics Express **32,** 32564–34153 (2014).

[14] N. B. e. Sá, Y. Sun, and J. Peatross, "Coherence effects in nonlinear Thomson scattering by electrons born from the same atom," Phys. Rev. A **110,** 043508 (2024).

[15] M. V. Ammosov, N. B. Delone, and V. P. Krainov, "Tunnel ionization of complex atoms and of atomic ions in an alternating electromagnetic field," Soviet Journal of Experimental and Theoretical Physics **64,** 1191 (1986).

[16] L. Richey, B. Stewart, and J. Peatross, "Creating and Analyzing a Mirage," The Physics Teacher **44,** 460–464 (2006).

[17] J. Madsen, L. Hancock, S. Voronov, and J. Peatross, "High-Order Harmonic Generation in Crossed Laser Beams," J. Opt. Soc. Am. B **20,** 166–170 (2003).